Volume 54
Number 9
7 May 2025
Pages 4089–4618

Chem Soc Rev

Chemical Society Reviews

rsc.li/chem-soc-rev

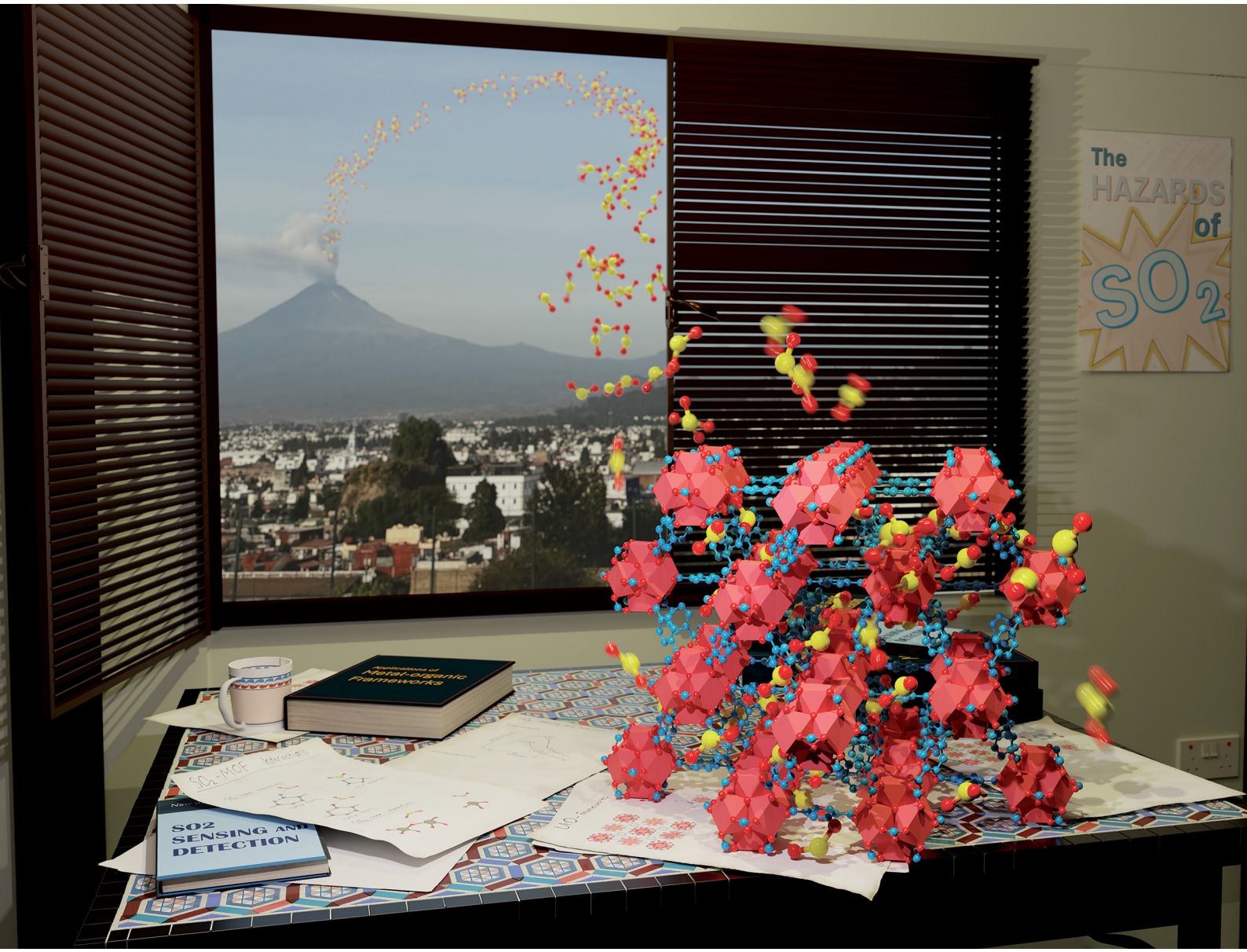

ISSN 0306-0012

ROYAL SOCIETY OF CHEMISTRY

REVIEW ARTICLE

Michael T. Huxley, Diego Solis-Ibarra, Ilich A. Ibarra, Christoph Janiak *et al.*

Metal–organic frameworks (MOFs) toward SO_2 detection

Chem Soc Rev

REVIEW ARTICLE

View Article Online
View Journal | View Issue

Cite this: *Chem. Soc. Rev.*, 2025, **54**, 4135

Metal–organic frameworks (MOFs) toward SO_2 detection

Juan L. Obeso, [ab] Catalina V. Flores, [ab] Ricardo A. Peralta, [c] Margarita Viniegra, [c] N. Martín-Guaregua, [c] Michael T. Huxley,*[d] Diego Solis-Ibarra, *[a] Ilich A. Ibarra *[a] and Christoph Janiak *[e]

Developing technology that can precisely monitor specific air pollutants in diverse settings is essential to control emissions and ensure safe exposure limits are not exceeded. Metal–organic frameworks (MOFs) are crystalline organic–inorganic hybrid materials, which are promising candidates for SO_2 detection. Their chemically mutable periodic structure confers outstanding surface area, thermal stability, and a well-defined pore distribution. Moreover, MOFs have exhibited extraordinary performance for SO_2 capture. Therefore, research has focused on their possible applications for SO_2 sequestration due to the selective and robust chemical and physical interactions of SO_2 molecules within MOFs. The variable SO_2 affinity presented by MOFs enables the adsorption mechanism and preferential adsorption sites to be resolved. However, for MOF-based SO_2 detection, selective SO_2 capture at shallow partial pressure (0.01–0.1 bar) is required. Thus, capturing SO_2 at low concentration is crucial for SO_2 detection, where textural properties of MOFs, mainly the pore-limiting diameter, are essential to achieve selective detection. In this review, we discuss the fundamental aspects of SO_2 detection in MOFs, providing a step-by-step methodology for SO_2 detection in MOFs. We hope this review can provide valuable background around SO_2 detection in MOFs and inspire further research within this new and exciting field.

Received 29th October 2024

DOI: 10.1039/d4cs00997e

rsc.li/chem-soc-rev

1. Introduction

The environmental and health implications of volatile pollutants pose major technological and economic challenges to modern society. The role of anthropogenic CO_2 and methane emissions in promoting an enhanced greenhouse effect is no doubt the most publicized example, yet lesser known pollutants such as carbon monoxide (CO), tropospheric ozone (O_3), ammonia (NH_3), volatile organic compounds, hydrogen sulfide (H_2S), and sulfur dioxide (SO_2) are harmful and prevalent in their own right.[1] These toxic gases contribute to poor health outcomes, crop damage, acidification of soils and waters, and the loss of biodiversity.[2,3] Therefore, targeting emissions and remediating contaminated areas remains a principal goal of governments worldwide.

The developed world's accelerating demand for energy,[4] which is still predominantly satisfied by fossil fuels, represents the major anthropogenic source of volatile pollutants.[5] Natural sources, such as volcanic activity, are a further contributing factor.[6] For example, México hosts several of the world's largest and most frequently active volcanoes. Volcanic gas emissions from these and other volcanoes are damaging to both the environment and human health in localized areas.[7,8]

Of the pollutants identified above, SO_2 is particularly hazardous due to a combination of toxicity and its ubiquity in flu gas emissions and various industrial settings. SO_2 is a colourless, irritating, and non-flammable gas with a strong odor that can be absorbed through the respiratory system or dermal contact.[9] It is classified as one of the most hazardous gases: exposure can to concentrations exceeding 100 ppm can be fatal in minutes.[10] However, even at lower concentrations, inhalation can cause severe respiratory complications.[11,12] The maximum daily average concentration for human exposure to SO_2 is 20 μg m^{-3} (8 ppb). Therefore, based on environmental and human health considerations, it is necessary to enforce stringent SO_2 emission regulations and prioritize the detection of SO_2 in both ecological and workplace settings.[13]

[a] *Laboratorio de Fisicoquímica y Reactividad de Superficies (LaFReS), Instituto de Investigaciones en Materiales, Universidad Nacional Autónoma de México, Circuito Exterior s/n, CU, Coyoacán, 04510 Ciudad de México, Mexico. E-mail: diego.solis@unam.mx, argel@unam.mx*

[b] *Instituto Politécnico Nacional, Centro de Investigación en Ciencia Aplicada y Tecnología Avanzada, Legaria 694, Col. Irrigación, Miguel Hidalgo, 11500 Ciudad de México, Mexico*

[c] *Departamento de Química, División de Ciencias Básicas e Ingeniería. Universidad Autónoma Metropolitana (UAM-I), 09340, Mexico*

[d] *School of Physics, Chemistry and Earth Sciences, Faculty of Sciences, Engineering and Technology, The University of Adelaide, Adelaide, South Australia 5005, Australia. E-mail: michael.huxley@adelaide.edu.au*

[e] *Institut für Anorganische Chemie und Strukturchemie, Heinrich-Heine-Universität Düsseldorf, 40204 Düsseldorf, Germany. E-mail: janiak@uni-duesseldorf.de*

1.1 Physicochemical properties of SO_2

To understand the challenges associated with the capture and detection of SO_2, the chemical and physical properties of the compound must be considered.[14,15] Valence shell electron pair repulsion theory predicts SO_2 to possess a bent geometry with an approximately 120° angle between the central sulfur and peripheral oxygen atoms (Fig. 1a). The bonding in SO_2 can be described with mesomeric bonds: a covalent S═O double bond and an ionic S^+–O^- bond (Fig. 1b). The molecule is polar (dipole moment 1.63305 D or 5.4473×10^{-30} C m) and is therefore soluble in water (Fig. 1c).[16] The S–O bond length in SO_2 is 1.43 Å, commensurate with the bonding models described above.[17]

1.2 Sources of SO_2 pollution

The SO_2 pollution is directly related to industrial activities associated with burning fossil fuels and biomass by power plants and chemical industries. This can include metal extraction from mines, locomotives, vehicles, and volcanos.[18] In general, power plants generate electricity *via* combustion, which releases SO_2 because the feedstocks contain sulfur compounds.

Therefore, industrial cities are confronted with an SO_2 pollution problem. Jion *et al.*[19] reported that 27.6% of SO_2 emissions in Asian countries arise from coal burning, while industry accounts for 20.7%, fossil fuel and biomass burning 13.8%, power plants and brick kilns 10.3%, and domestic production 3.4%. The increase in SO_2 pollution is related to industrialization, urbanization, and economic development. Specifically, the SO_2 concentration observed in several Asian countries is relatively high. For example, at Langkawi Island, Malaysia, the concentration is 14 ppb (data from 1999–2011)[20] while in Lahore City, Pakistan, it is 19.11 ± 6.18 ppb.[21] For Longfengshan, Shangdianzi, Houma, Huaian, Lin'an, kaili,

Juan L. Obeso

Juan L. Obeso was born in Sinaloa, Mexico. He obtained a BSc in chemical engineering at Universidad Autónoma de Sinaloa in 2019 and an MS at Instituto Politécnico Nacional in 2021. He is currently a PhD student at Instituto Politécnico Nacional and Universidad Nacional Autónoma de México under the supervision of Prof. Ilich Ibarra. His research interests mainly focus on MOF synthesis, catalysis, adsorption, and detecting water and toxic pollutants.

Margarita Viniegra

She earned her PhD in Chemistry from the Universidad Autónoma Metropolitana (UAM) and completed a postdoctoral fellowship at the Institute of Physics at the Universidad Nacional Autónoma de México. Since 1982, she has served as a professor at UAM. Her research interests in heterogeneous catalysis focus primarily on transition metals and their oxides. In recognition of her teaching excellence, she was awarded the UAM-I Teaching Award in 2010. She has held several leadership roles, including Head of the Department of Chemistry, Coordinator of both Undergraduate and Graduate Studies, President of the Academy of Catalysis A.C., and President of the National Council for the Evaluation of Chemical Sciences Programs.

Michael T. Huxley

Michael Huxley was born in Adelaide, South Australia. He completed his undergraduate studies at The University of Adelaide, completing a PhD in Chemistry under the supervision of Prof. Christian Doonan and Prof. Christopher Sumby in 2018. Michael's research interests focus on catalysis in MOFs and elucidation of chemical processes within MOF matrices. He is presently an Associate Lecturer in chemistry at The University of Adelaide.

Diego Solis-Ibarra

Diego Solis-Ibarra obtained his Chemistry degree from UNAM in 2008 and completed his PhD in 2012 under the supervision of Prof. Vojtech Jancik. He conducted research stays at UC Santa Barbara and MIT before joining Stanford University as a postdoctoral researcher in Prof. Hemamala Karunadasa's group. In 2015, he returned to UNAM, where he is now an Associate Professor and serves as the Director of the Institute for Materials Research. His research focuses on hybrid materials for sensing, photovoltaics, and optoelectronics.

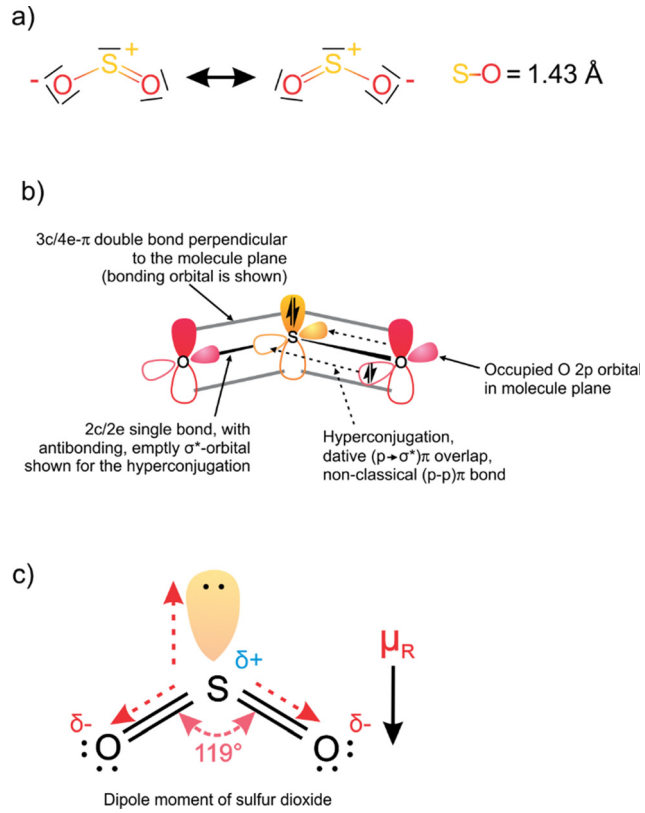

Fig. 1 (a) Valence bond resonance SO_2 structure, (b) scheme displaying the molecular orbital bonding model for SO_2, (c) SO_2 dipole moment.

Chenzhou, Meixian, Dianbai of China is 23.59 ± 23.97 ppb (data from 2010).[22] In rural sites in China is 21.06 ± 9.23 ppb (data from 2007–2008).[23] Furthermore, Mousavi *et al.*[24] reported an analysis of the SO_2 concentration arising from flares at the Maroon gas refinery located in the suburb of Ahvaz, Iran. It was found that the SO_2 concentration rises to 82.1 ppb during the cold season.

1.3 Industrial uses for SO_2 and existing capture technologies

SO_2 finds multifarious industrial uses. For example, the remarkable antiseptic and antioxidant properties of SO_2 have led to its frequent use as a food and beverage preservative,[25] particularly in winemaking, where it acts as an antimicrobial agent during the aging and storage of wine.[26] In the chemical industry, SO_2 is an intermediate in the production of sulfuric acid (H_2SO_4). The industrial synthesis of H_2SO_4 takes place by first transforming sulfur into SO_2 using O_2 as an oxidant, followed by the conversion of SO_2 into sulfur trioxide (SO_3) using vanadium and alkali oxides.[27] The resulting SO_3 is dissolved in 98 wt% H_2SO_4 solution to generate a 99.7 vol% H_2SO_4 solution.[28] SO_2 is also employed as a bleaching agent[29] and was a first-generation refrigerant due to its high heat of evaporation.[30]

Indeed, industrial demand for SO_2 and inadvertent emission from coal-fired power stations necessitates strict control for safety and environmental reasons. Considering the need to limit anthropogenic SO_2 emissions, significant investment has been expended toward SO_2 capture at point sources such as coal-fired power stations. The first SO_2 capture system, the spiral-tile packed tower, was developed in the early 1930s[31–33] but is highly inefficient due to the consumption of vast quantities of water during its operation. The process also produces large quantities of sulfuric acid contaminated water.[34]

SO_2 scrubbing, also known as flue-gas desulfurization (FGD).[35] FGD is employed using either a once-through or regenerative process. In the former, the spent sorbent (which is calcium sulfate) can be used in the construction industry or otherwise disposed. The regenerative process is more desirable because the sorbent is re-activated, and SO_2 is recovered for use in chemical industries. Despite this process being widely applied and largely successful in mitigating the worst impacts of acid rain, FGD systems still release significant quantities of SO_2 into the atmosphere.[36] Therefore, interest has been garnered by alternative processes such as the use of ceramic

Ilich A. Ibarra

Ilich Ibarra was born in Mexico City, Mexico in 1981. He completed a BSc in chemistry at UAM (Mexico) in 2005. In 2010 he obtained his PhD in Chemistry at Nottingham University (UK). He then took a postdoctoral position, in 2010, at UT Austin (USA). In 2013 he was awarded as a Wenner-Gren researcher at SU (Sweden). In 2020 he was awarded with the Young Investigators Award in Exact Sciences by the Mexican Academy of Sciences. In 2024 he was promoted as Full Professor at UNAM.

Christoph Janiak

Christoph Janiak is full professor for Nanoporous and Nanoscale Materials at the Heinrich Heine University of Düsseldorf since 2010, with research interests in the synthesis and properties of metal and porous organic frameworks (MOFs, COFs), mixed matrix membranes, metal nanoparticles, ionic liquids, and catalysis. He is currently an honorary professor at Wuhan University of Technology and guest professor at the Hoffmann Institute of Advanced Materials at Shenzhen Polytechnic University in China. He has (co-)authored about 730 research papers (H index 91) and is a Fellow of the Royal Society of Chemistry (FRSC).

hollow fiber membranes filled with various aqueous solutions to capture SO_2.[37–40] Finally, various 'wet-sulfuric acid' processes have been used extensively for sulfur removal since the 1980s,[41] motivated in part by the generation of valuable byproducts.[42]

1.4 Emerging technologies for SO_2 capture

The aforementioned processes generate large quantities of wastewater, corrode pipelines, impose significant economic costs, and leave residual traces of SO_2.[43] Thus, as an alternative, solid-state adsorbents have received growing interest. For example, zeolites and metal oxides have been investigated for SO_2 uptake.[44,45] Zeolites are widely used as adsorptive materials, ion exchangers, and catalysts.[46] Zeolites present attractive qualities in adsorption applications, including low-cost synthesis, relatively high surface area, microporosity, and thermal and mechanical stability.[47] However, zeolites exhibit drawbacks associated with their regeneration process. In some cases, the strong host–guest interaction between a zeolite and gas molecule invokes chemical bonding,[48] necessitating thermal activation (200 °C) under vacuum to regenerate the adsorbent and increasing operating costs.[49] Similarly, metal-oxides offer advantageous properties for adsorption applications but often form non-reversible interactions with gases of interest.[50]

Therefore, new porous materials have been investigated with a focus on sustainable development and real-world applications.[51,52] This includes a new generation of organic or hybrid organic–inorganic adsorbent materials such as metal–organic cages (MOCs),[53] porous organic cages (POCs),[54] and metal–organic frameworks (MOFs).[55] The latter are crystalline, typically microporous materials constructed from metal ions interconnected by organic linkers, forming two or three-dimensional coordination networks.[56,57] MOFs feature tunable physicochemical properties due to reticular design principles, narrow pore size distributions, high surface areas, and in some instances, chemical and thermal stability.[58,59] Their metal and linker building blocks allow the design of a tremendous range of different MOFs which can be tuned *via* reticular synthesis to suite specific applications. These properties have conferred significant advantages in adsorption,[60–63] catalysis,[64–66] drug delivery,[67,68] separation,[69,70] and proton conductivity[71,72] applications.

Only a limited number of chemically stable MOFs have so-far exhibited promising SO_2 adsorption properties. This paucity reflects the often-poor stability of coordination clusters – central to the structural integrity of MOFs – towards SO_2 exposure.[73] During adsorption, SO_2 molecules interact with MOFs *via* chemical or physical adsorption, depending on the nature of the binding sites available in the framework. The stability of MOFs towards SO_2 is dependent on the strength of the metal–ligand coordination bond (ranging between 300 kJ mol^{-1} to 600 kJ mol^{-1} for carboxylate linkers) and coordination number of the metal node.[74,75] Displacement of metal-linker bonds by SO_2 leads to decomposition of the MOF sorbent. Since linkers are classified as electron-donating species and metal ions are electron-accepting species,[76] Pearson's hard-soft acid–base (HSAB) concept provides a rationale for the stability of MOFs. Hard bases establish stronger bonds with hard acids and soft acids with soft bases.[77]

Based on these principles, a range of chemically stable MOFs have been synthesized and found to exhibit high SO_2 uptakes.[78] Chemical stability is, however, only one of the challenges facing chemists as they work to establish an industrial role for MOFs. Criticism frequently centers around the high cost of MOF linkers as well as the scalability of MOF synthesis, leading to questions about the economic feasibility of industrial-scale SO_2 capture (and that of other gases such as CO_2) using MOFs.[79] Indeed, the feasibility of adsorptive SO_2 capture with MOFs at scale remains uncertain. However, laboratory scale results for MOF-based SO_2 removal suggest that other applications that require smaller quantities of adsorbent, particularly SO_2 detection rather than capture, are promising avenues for MOF research.

1.5 Principals for SO_2 detection

Detecting a specific molecule relies on stimulating a specific response in the sensor, which, when measured, gives either a quantitative or qualitative measure of the concentration (or presence) of the analyte.[80,81] Since MOFs are naturally suited to sensing applications due to their intrinsic porosity and functional versatility, a wide range of MOF based sensing techniques have been envisaged.[82] These include MOF-based chemiresistive sensors,[83] luminescent sensors,[84] colourimetric sensors,[85] and magnetic sensors.[86] MOF-based chemo resistive materials are based on the change in resistance in response to a chemical surface reaction or adsorption of a guest molecule.[87] Sensors based on luminescence response employ the change in luminescence properties of certain MOFs, which generate a turn-on or, more often, turn-off fluorescence response.[88,89] Furthermore, some MOFs exhibit a characteristic shift in their emission wavelength(s) when exposed to specific molecules such as ammonia.[90] Colourimetric detection is used for simplicity and can be performed *via* visual analysis.[91] Additionally, the spin-crossover (SCO) effect has gained interest in the scientific community for its applications in magnetic sensors. In MOFs for instance, exposure to external stimuli such as temperature, pressure or magnetic field can induce measurable changes in the spin state of framework metal ions (typically Fe(II) framework nodes).[92,93] However, guest molecules can also induce a spin transition, which can be exploited for the purpose of detection.[94] These techniques have been combined to detect various small molecules, including organic solvents,[95] aqueous pollutants,[96] greenhouse gases,[97] and acidic solvents.[98] However, SO_2 detection has received limited attention.

Presently available SO_2 detectors employ an electrochemical system based on a solid polymer, usually polycarbonate. In such devices, an electrochemical reaction occurs, generating an electron in the working electrode, which produces an electrical current that is proportional to the SO_2 concentration. The SO_2 detection range is from 0 to 20 ppm with a response time of 30 s.[99,100] Such devices are frequently used in coal mines and the petroleum and chemical industries where SO_2 is encountered. However, drawbacks associated with existing SO_2 detectors,

including interference from other gases, and sensitivity towards temperature and humidity fluctuations which lead to low sensitivity and accuracy.[101–103]

SO_2 detectors can be improved by introducing new solid-state materials with increased selectivity towards SO_2. Therefore, considering the promising SO_2 adsorption properties of MOFs, SO_2 detection is a logical next step. SO_2 tolerant MOFs have shown moderate to high SO_2 uptake. Intuitively, materials with a high SO_2 affinity – interpreted as evidence for an enhanced interaction between SO_2 and the MOF framework – could be promising candidates for detection applications.[104] To exploit this potential, it is necessary to understand the fundamental interactions between SO_2 molecules and the MOF. By transforming these host–guest interactions into measurable signals, the presence and, in some cases, concentration of SO_2 can be reliably determined. To meet this goal, researchers must draw on the vast wealth of research which has characterized the structure–property relationships of MOFs and optimized their mechanical and chemical stability – both crucial properties for real-world applications where MOFs are incorporated into functional devices. The accelerated development of MOFs to improve their properties for gas detection is crucial for building functional devices.

Thus, this review provides a comprehensive summary and analysis of MOF-based SO_2 detection strategies. To provide a suitable background, seminal examples of MOF-based detection of sulfur compounds other than SO_2 (and also in solution) are also provided. We emphasize the relationship between specific characteristics of porous materials (*i.e.*, surface area, pore volume, pore diameter, and functionalisation), which combine with the molecular properties of SO_2 to provide a means for reliable detection. The primary techniques with which SO_2 detection is studied in MOFs are discussed in detail. We aim to encourage further investigation into the exciting field of MOF-based environmental remediation and sensing applications.

2. MOFs for SO_2 capture

One of the primary purposes of this review is to explore existing – and postulate promising – MOF candidates for detecting SO_2. Therefore, the characteristic properties shared by MOFs that exhibit a high affinity towards SO_2 must be examined so that these desirable properties can be refined for SO_2 detection applications.

2.1 Main interactions of the SO_2 molecule within MOFs

The host–guest interaction between SO_2 molecules and MOFs provides a fundamental basis for understanding the application of MOFs in SO_2 detection. Considering the chemical diversity of MOF pores, it is necessary to establish the potential modes by which SO_2 can interact with adsorbents.

The adsorption of gases on surfaces is divided into two limiting processes: (i) physisorption, that is, physical adsorption, which displays weak gas–sorbent interactions comprising van der Waals forces, reversibility and a low heat of adsorption (<50 kJ mol^{-1}); and (ii) chemisorption, that is, chemical adsorption, which exhibits comparatively strong interactions characteristic of chemical bonding, a high heat of adsorption (>50 kJ mol^{-1}), and less facile reversibility.[105] From this point of view, SO_2 adsorption processes are governed by the chemistry of available adsorption sites within a MOF, which determines the type and strength of interactions.

Preferential adsorption sites within MOF structures (Fig. 2a) can include hydroxyl/amino groups, open metal sites (including defects and missing linkers), and halogen/methyl groups.[106] Thus, the extraordinary chemical diversity available in MOFs gives rise to a range of possible interactions with polar SO_2 molecules (Fig. 2b), including hydrogen bonding, direct coordination to framework metal ions, sulfur–halogen bonding, S–π interactions, and other electrostatic interactions.[107–109]

When coordinating to metal centres, such as open metal sites in MOFs, an SO_2 molecule can exhibit multiple binding modes that employ both oxygen and sulfur donors. Typical SO_2 coordination modes are summarized in Fig. 2c and include (i) η^1-SO_2, planar and S-bonded, (ii) η^1-SO_2, pyramidal and S-bonded, (iii) η^2-SO_2, both S and O-bonded, and (iv) η^1-SO_2, O-bonded.[111] These metal–SO_2 coordination modes have been exploited to improve SO_2 adsorption in MOFs at open metal centres.

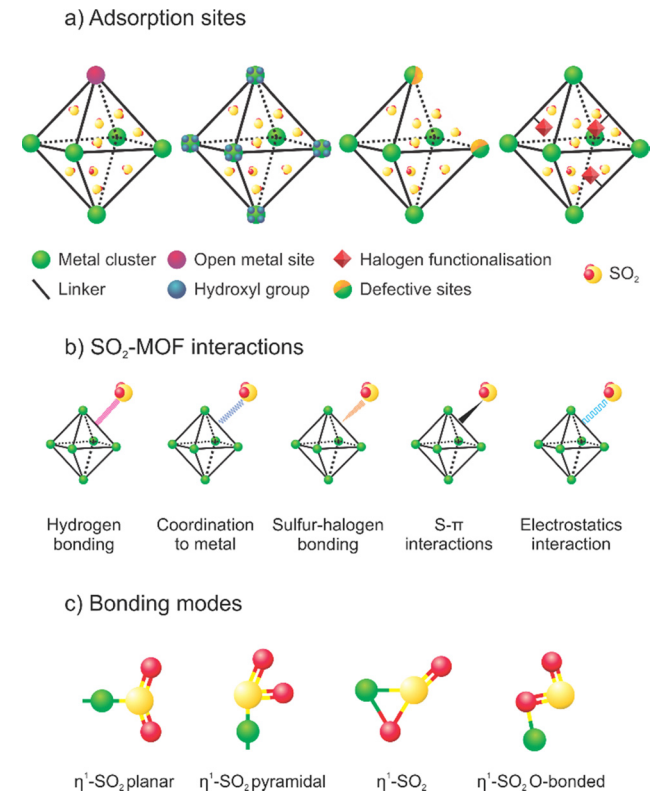

Fig. 2 (a) Main adsorption sites in MOF, (b) summary of possible SO_2–MOF interactions, and (c) metal bonding modes of the SO_2 molecule depicted schematically. Based on ref. 106,110.

Metal centres do not comprise the only sites with which SO_2 can interact within MOFs. Hydrogen bond donors are a common preferential adsorption site in MOFs, particularly in the form of hydroxyl and amine moieties. The hydroxido, hydroxo, or hydroxy group is an intrinsic characteristic of numerous MOFs bearing cluster-based SBUs, where, for instance, the μ-OH moieties bridge two or three metal centers.[112] Amino groups on the other hand are provided *via* suitably functionalized organic linkers.[113] The interaction between SO_2 molecules and hydroxy sites in a MOF was first directly identified in 2012 by Yang *et al.*[114] in NOTT-300(Al) (later renamed MFM-300(Al), linker BPTC)[115] using *in situ* powder X-ray diffraction (PXRD), inelastic neutron scattering, and grand canonical Monte Carlo (GCMC) simulations. The NOT-300(Al) structure features μ-OH groups, which bridge between Al(III) ions to form infinite 1D chains that extend along the MOF pores and are bridged by BPTC moieties. Comprehensive analysis revealed that SO_2 molecules engage in hydrogen bonds ($SO_2(O)\cdots H(OH)$ = 2.376(13) Å) with μ-OH sites (Fig. 3a), supported by complementary interactions with aromatic C–H sites of adjacent linkers. Five hydrogen bond interactions were observed between the host framework and bound SO_2. Furthermore, the SO_2 molecules bound to the framework interact *via* dipole–dipole $S\cdots O$ interactions ($S\cdots O$ = 3.34(7) Å) with secondary SO_2 molecules located within the MOF pore (Fig. 3b). A follow-up study published in 2020 established the long-term stability of NOT-300(Al) towards SO_2, NH_3, and NO_2. This study highlighted the capacity of diffraction techniques to precisely elucidate the interaction mechanisms behind SO_2 adsorption in robust, crystalline adsorbents.

MFM-300(Sc), which is isostructural to MFM-300(Al) (previously named NOT-300(Al) as described above), exhibits infinite 1D [Sc_2(μ-OH)] chains interconnected by BPTC moieties. SO_2 interactions were elucidated using GCMC simulations, which revealed that SO_2 molecules engage in hydrogen bonding with μ-OH sites situated along the inorganic node.[116] The indium analog MFM-300(In) displayed high selectivity for SO_2 over N_2, CH_4, and CO_2. *In situ* PXRD revealed similar behavior to that observed in MFM-300(Al): SO_2 occupies two adsorption sites. One molecule interacts with a bridging hydroxyl group [$SO_2(O)\cdots H(OH)$ = 3.17 Å] while at the same time, a second SO_2 molecule is supported in the MOF pore *via* dipole–dipole $S\cdots O$ interactions with the bound SO_2 molecule. Inelastic neutron scattering experiments probed the interaction between N_2, CO_2, and SO_2 gas molecules and μ-OH sites. A substantial shift in signals associated with wagging/bending modes of aromatic C–H bonds and bridging μ-OH sites was observed upon exposure to SO_2. A less significant shift was observed upon CO_2 adsorption, confirming that SO_2 adsorption is associated with stronger hydrogen bonding interactions with these framework sites.[117] Further spectroscopic evidence for the hydrogen bonding interaction was provided by monitoring the ν(OH) band at 3657 cm^{-1}. These studies validate the role of hydrogen bonding between SO_2 and inorganic hydroxyl sites and intermolecular SO_2–SO_2 interactions in stabilizing adsorbed SO_2 in robust MOFs.

Similar interactions have been described for various μ-OH bearing MOFs. For example, rigid MIL-53(Al)-TDC (TDC = 2,5-thiophenedicarboxylate) and the flexible MIL-53(Al)-BDC displayed this characteristic interaction.[118] DFT simulations were employed to probe the SO_2/MOF host–guest chemistry. SO_2 was observed to interact through hydrogen bonding with the μ-OH group of both MIL-53(Al)-TDC and MIL-53(Al)-BDC (with a mean $SO_2(O)\cdots H(OH)$ separation distance of 2.05 Å and 1.78 Å, respectively). The shorter hydrogen bonding interactions observed in the more flexible framework were related to adsorption-induced decrease in pore size in the flexible framework, facilitating stronger hydrogen bonding interactions. Multiple steps in the SO_2 adsorption isotherm supported this flexible behavior. Furthermore, the strong affinity for SO_2 molecules at the μ-OH site leads to a remarkable selectivity over a wide range of gases. Another framework bearing bridging μ-OH groups, DUT-4[119] (with the linker NDC), displays relatively high SO_2 adsorption (13.6 mmol g^{-1} – compared to 8.9 mmol g^{-1} for MIL-53(Al)-TDC and 0.8 mmol g^{-1} for MIL-53(Al)-BDC) at 298 K and 1 bar).[118] DFT studies show that SO_2 interacts with the μ-OH group and the linker (distance of 2.9 and 2.7 Å, respectively). The affinity towards the μ-OH group contributed to selective adsorption of SO_2 over CH_4. Furthermore, the μ-OH bearing framework, Mn-CUK with the linker PDCA = 2,4-pyridinedicarboxylate, contains a [$Mn_3(\mu_3\text{-OH})_2$] cluster and displays moderate SO_2 adsorption capacity (5.51 mmol g^{-1}) at 298 K and 1 bar.[120] Variable-temperature SCXRD studies suggested that SO_2 binds *via* hydrogen bonding with the μ_3-OH sites.

MIL-160 (with the linker FDCA = 2,5-furandicarboxylate) is a furan-based MOF with a moderate SO_2 uptake (7.2 mmol g^{-1}) at 293 K and 0.97 bar.[121] However, the framework displays high selectivity towards SO_2 over CO_2, CH_4, N_2, and H_2. The feasible binding sites for SO_2 in MIL-160 were identified by DFT calculations using geometry optimization of SO_2 within the pores (Fig. 4a–c). Three main interactions were found to occur between MIL-60 and SO_2: dipole–dipole bonding at furan oxygen sites ($SO_2(S)\cdots O$(furan) distance 3.27 Å), hydrogen

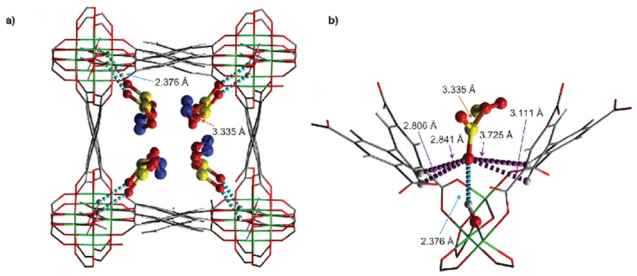

Fig. 3 (a) View of the crystal structure of NOTT-300·4.0-SO_2 obtained from Rietveld refinement of data on SO_2-loaded material at 1.0 bar. The adsorbed SO_2 molecules in the void are highlighted using a ball-and-stick represention. The sulfur atom of the second site of SO_2 is highlighted in blue. (b) Detailed view of the OH and CH contact with SO_2 molecules in a distorted pocket-like cavity. (Aluminum, green; carbon, grey; oxygen, red; hydrogen, white; sulfur, yellow.) (Reprinted (adapted) with permission from ref. 114 Copyright (2012) Springer Nature).

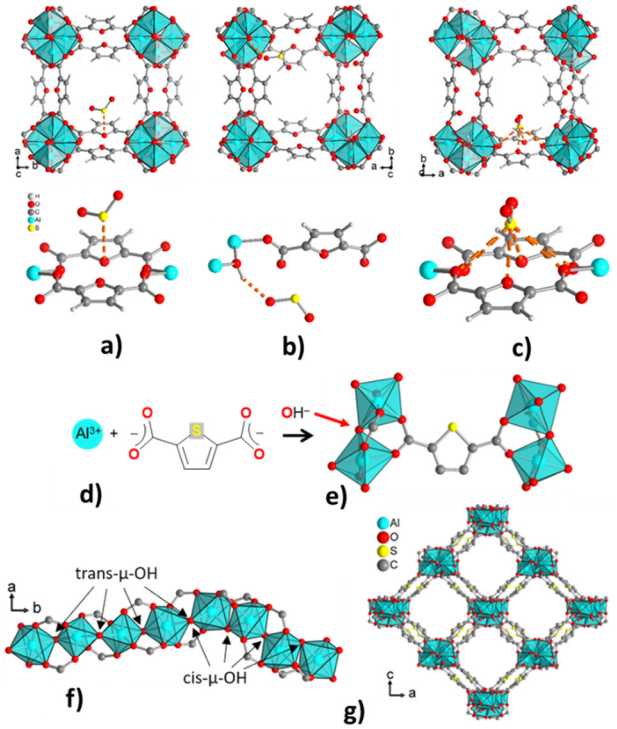

Fig. 4 DFT-simulated binding sites of SO_2 in MIL-160. (a) $O_{furan}\cdots S_{SO_2}$ interaction, (b) $OH_{Al\text{-}chain}\cdots O_{SO_2}$ interaction, and (c) $O_{furan/carboxylate}\cdots S_{SO_2}$ interaction. (Reprinted with permission from ref. 121 Copyright (2019) American Chemical Society). Crystal structure of CAU-23: (d) Al^{3+}, 2,5-thiophenedicarboxylate (TDC^{2-}) and hydroxide ions as building blocks, (e) TDC^{2-} linker coordination to {AlO_6} octahedra, (f) chains composed of alternating segments of four helical *cis*- and four *trans*-corner sharing {AlO_6} octahedra, (g) section of the packing diagram with the {AlO_6} chains connected by the TDC^{2-} linkers to yield square-shaped channels. (Reprinted with permission from ref. 122 Copyright (2022) with permission from John Wiley & Sons).

bonding at μ-OH ($SO_2(O)\cdots H(OH)$ distance 2.10 Å), and finally, dipole–dipole bonding between SO_2 and two furan units (distances of 3.15 and 3.36 Å). The short $SO_2(O)\cdots H(OH)$ hydrogen bond contact implies a high affinity between SO_2 and the hydroxyl sites which contributes to the outstanding selectivity toward SO_2.

Similarly, CAU-23 (with the linker TDC) displays *cis* and *trans*-μ-OH sites in the inorganic building unit (Fig. 4d–g) and has been evaluated for gas sorption properties.[122] CAU-23 shows a relatively high SO_2 adsorption capacity (8.4 mmol g^{-1}, at 1 bar and 293 K) and low CO_2 and CH_4 adsorption capacity (3.97 mmol g^{-1} and 0.89 mmol g^{-1}, respectively, all at 1 bar and 293 K). Moreover, the presence of *cis* and *trans*-μ-OH groups imparts a high affinity towards polar SO_2 molecules over CO_2, H_2, and CH_4. Further to the behavior described above, adsorbed SO_2 can also interact favorably with the π-system and S atom from the linker.

Coordinatively unsaturated sites can be generated in MOFs at the framework nodes when coordinated solvent (*i.e.*, water) is dissociated during thermal activation, leaving behind an accessible Lewis acidic metal site.[123,124] This attribute has drawn considerable interest in the adsorption and catalysis fields.[125,126] M-MOF-74 (with the linker DHTP = 2, 5-dihydroxyterephthalate) (M = Zn and Mg) is one such material and displays strong interactions between adsorbed SO_2 and open metal sites generated during activation.[127] Using *in situ* infrared spectroscopy and *ab initio* DFT calculations, the first preferential adsorption site was identified as a direct $SO_2(O)$–M interaction. Another MOF, MFM-170, features well-defined Cu(II) sites which also interact directly with SO_2. MFM-70 consists of a $[Cu_2(O_2CR)_4]$ (O_2CR = 4′,4‴-(pyridine-3,5-diyl)bis([1,1′-biphenyl]-3,5-dicarboxylate) dimer with four linker carboxylate moieties occupying the equatorial sites and one linker *N*-pyridyl donor coordinating to one of the two axial sites of the dimer (the second being available for guest coordination).[128] This available Cu(II) coordination site facilitates reversible SO_2 capture, while the structure remains stabile even towards exposure to wet SO_2. Using *in situ* SCXRD, FTIR microspectroscopy, and inelastic neutron scattering, the open Cu(II) sites were confirmed to act as $SO_2(O)$–Cu adsorption sites. The Cu(II) framework, MFM-190 (linker: 5,5′-(pyridine-2,5-diyl)diisophthalate), also exhibits open Cu^{2+} sites which form the primary adsorption site for SO_2.[129] Furthermore, an S–π interaction was observed between SO_2 and delocalized π systems of the two neighboring phenyl rings. *In situ* neutron powder diffraction, inelastic neutron scattering, and synchrotron infrared microspectroscopy studies revealed the location of host–guest binding. The MOF MIL-101(Cr)-4F(1%) is a partially fluorinated MOF from the MIL-101(Cr) family. This Cr(III)-based MOF was synthesised by mixing BDC and 2,3,5,6-tetrafluoro-1,4-benzenedicarboxylate (BDC-4F), thereby doping the structure with fluorine (MIL-101(Cr)-4F(1%) = $[Cr_3O(BDC)_{2.91}(BDC\text{-}F4)_{0.09}]Cl$).[130] The presence of fluorine modulates the pore-surface electron density leading to considerably improved SO_2 capture due to the enhanced dipole–dipole interactions with the pore surface.

Defect sites in MOFs – such as missing linker or missing cluster defects, which are prominent in Zr(IV) frameworks, among many others[131,132] – are correlated with a decrease in the chemical stability of the framework but provide new interaction sites for adsorbate molecules, including SO_2.[133] The MOF $[Ni_8(OH)_4(H_2O)_2(BDP\_X)_6]$,[134] (where H_2BDP_X = 1,4-bis(pyrazol-4-yl)benzene-X with X = H (1), OH (2), NH_2 (3)) (Fig. 5a), was post-synthetically modified by placing the material in ethanolic solutions of potassium hydroxide to generate the defect rich frameworks $K[Ni_8(OH)_3(EtO)_3(BDP\_X)_{5.5}]$ (1@KOH, 3@KOH) and $K_3[Ni_8(OH)_3(EtO)(BDP\_O)_5]$ (2@KOH). The defective frameworks were soaked in aqueous $Ba(NO_3)_2$, leading to exchange of extra-framework potassium ions for Ba(II), giving $Ba_{0.5}[Ni_8(OH)_3(EtO)_3(BDP\_X)_{5.5}]$ (1@$Ba(OH)_2$, X = H; 3@$Ba(OH)_2$, X = NH_2), and $Ba_{1.5}[Ni_8(OH)_3(EtO)(BDP\_O)_5]$ (2@$Ba(OH)_2$). The logical basis for this extensive post-synthetic modification was to imbue the defective frameworks with a greater capacity to interact with SO_2. Possible SO_2 interactions were evaluated by DFT calculations (Fig. 5b–e). The preferential SO_2 adsorption sites in 1@$Ba(OH)_2$ are the crystal defects where SO_2 coordinates in a bidentate fashion with Ba(II) ions. This is contrasted with 1@KOH wherein SO_2 coordinates through a

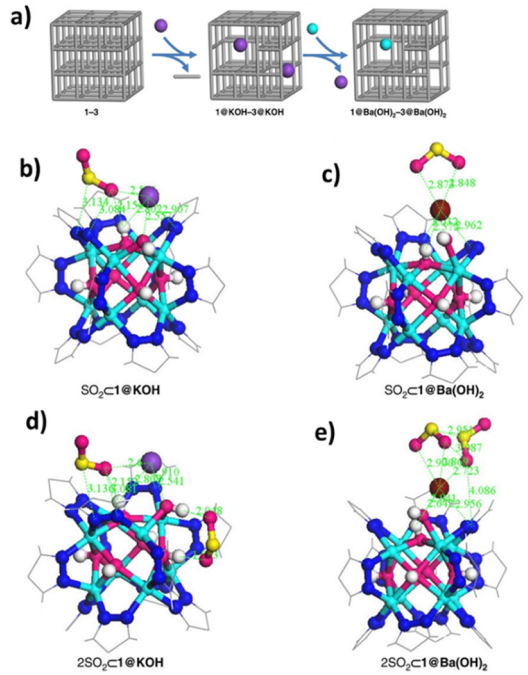

Fig. 5 (a) Schematic representation of the successive post-synthetic modifications, from pristine nickel pyrazolate $[Ni_8(OH)_4(H_2O)_2(BDP\_X)_6]$ (H_2BDP_X = 1,4-bis(pyrazol-4-yl)benzene-4-X with X = H (1), OH (2), NH_2 (3)) frameworks to yield the missing linker defective $K[Ni_8(OH)_3(EtO)_3(BDP\_X)_{5.5}]$ (1@KOH, 3@KOH) and $K_3[Ni_8(OH)_3(EtO)(BDP\_O)_5]$ (2@KOH) and subsequently, the ion-exchanged $Ba_{0.5}[Ni_8(OH)_3(EtO)_3(BDP\_X)_{5.5}]$ (1@$Ba(OH)_2$, X = H; 3@$Ba(OH)_2$, X = NH_2), and $Ba_{1.5}[Ni_8(OH)_3(EtO)(BDP\_O)_5]$ (2@$Ba(OH)_2$) materials. Organic linker (grey bar), potassium (purple), barium (cyan). Sulfur dioxide interaction with crystal defect sites. DFT structure minimization of the molecular configuration of one (b) and (c) and two (d) and (e) adsorbed SO_2 molecules on 1@KOH (left) and 1@$Ba(OH)_2$ (right) materials. (Reprinted (adapted) with permission from ref. 134 Copyright (2017) Springer Nature under a Creative Commons CC BY license).

less favourable monodentate mode with potassium ions. Ba(II) ions are therefore associated with enhanced interactions between SO_2 and the framework. The formation of missing linker defects, where hydroxide displaces framework linkers, also contributes since the hydroxyl moieties interact favorably with SO_2. Thus, this novel defect engineering methodology facilitated improved adsorption performance by producing defect sites with a high affinity towards SO_2 and improving the accessibility of the framework to sorbate due to the presence of missing linker defects.[134,135]

Finally, the installation of halogen atoms on organic linkers can enhance the gas capture performance of MOFs. For example, the HHU-2-X (X = Cl, I, and Br) family are halogen functionalized MOF-801 derivatives, which are composed of halofumarate linkers which bridge 12-connected $[Zr_6O_4(OH)_4]$ clusters.[136] These materials display moderate SO_2 uptake compared to pristine MOF-801 which shares the same *fcu* topology but an unfunctionalized fumarate linker. HHU-2-Cl for instance displayed an SO_2 adsorption capacity of 9.69 mmol g^{-1} at 296 K and 1 bar, while MOF-801 reaches only 8.00 mmol g^{-1} at 296 K and 1 bar. Halogen functionalisation increases the polarity of the MOF pores, improving the affinity towards polar SO_2 molecules over CO_2.

Thus, it is evident that the chemical functionality of MOFs directly affects their SO_2 affinity by modulating the SO_2 interaction mechanism. Preferential SO_2 adsorption sites range from μ-OH moieties involved in hydrogen bonding to coordinatively unsaturated metal centres where coordination chemistry can take place.[117,120] The studies highlighted so far have focused on SO_2 adsorption at relatively high pressure (1 bar). However, systems that detect SO_2 must possess strong and selective affinity towards the gas at much lower pressures.

2.2 Selective capture of SO_2 in MOFs

An important consideration for the effective MOF-based detection of SO_2 is high selectivity. The modular nature of MOFs provides opportunities to tune their frameworks *via* the incorporation of specific functional groups that preferentially interact with SO_2 over other molecules. One of the earliest investigations into selective SO_2 adsorption in MOFs was reported in 2008 by Britt *et al.*[137] Using kinetic breakthrough measurements the authors calculated the dynamic SO_2 adsorption capacity of MOF-5, IRMOF-3, MOF-74, MOF-177, MOF-199, and IRMOF-62. Remarkably, the pore functionality (*i.e.*, unsaturated metal sites and amino functionality) was found to play a dominant role in determining the dynamic SO_2 adsorption performance. Later, it was reported that the incorporation of urea within Zn(II)-based MOFs (achieved using the linker 6-oxo-6,7-dihydro-5*H*-dibenzo[*d*,*f*][1,3]diazepine-3,9-dicarboxylate),[138] provided enhanced hydrogen-bonding interactions with SO_2 over other gas molecules such as CO_2.

Savage *et al.*[117] demonstrated the utility of the hydroxo functional group (–OH) in promoting high SO_2 selectivity in MFM-300(In). The material exhibited remarkable selectivity (SO_2/CO_2 60, SO_2/CH_4 425, and SO_2/N_2 5000) under ambient conditions (*i.e.*, 50 : 50 mixture at 1 bar and 298 K). The origin of this behavior was investigated by combining crystallographic and spectroscopic techniques including inelastic neutron scattering; which revealed that enhanced supramolecular binding interactions – especially hydrogen bonding by the –OH functional group – are directly responsible for observed affinity towards SO_2. Using *in situ* synchrotron X-ray diffraction experiments, the same authors established the role of μ_3-O and μ_3-OH functional groups in the remarkable SO_2/CO_2 and SO_2/N_2 selectivity observed in MFM-601 (with the linker PPTA = 4,4′,4″,4‴-(1,4-phenylenebis(pyridine-4,2,6-triyl))tetrabenzoate).[139] The dipole moment of SO_2 interacts favorably with the μ_3-O and μ_3-OH groups within the pores of MFM-601, which explains the affinity between MFM-601 and polar SO_2 over non-polar CO_2 or N_2. MIL-160 is an Al(III)-based MOF which also exhibits high SO_2 uptakes at low pressures ($p < 0.01$ bar) and a remarkable selectivity towards SO_2 over CO_2 due to the presence of furan moieties which provide preferential binding sites for SO_2(O(furan)$\cdots$S(SO_2)).[121] Recently, the SO_2/CO_2 selectivity of NH_2-MIL-101(Cr), Basolite F300 (Fe-1,3,5-BTC), HKUST-1, ZIF-8 and ZIF-67 was evaluated in comparison to non-MOF

adsorbents Zeolite Y, SAPO-34, silica gel 60 and CTF-1,[140] concluding that Zeolite Y and CTF-1(600) showed the most promising SO_2/CO_2 selectivity results with an ideal adsorbed solution theory selectivity in the range of 265–149 and 63–43 with a mole fraction of 0.01–0.5 SO_2 at 293 K and 1 bar.

Using solid-state cationexchange, Mon *et al.*[141] post-synthetically modified a Ni(II)-based MOF (with the linker MPBA = *N*,*N*′-2,4,6-trimethyl-1,3-phenylenebis(oxamate)) to increase its N_2/SO_2 selectivity considerably. By soaking the MOF crystals in a saturated aqueous solution of $Ba(NO_3)_2$ for 48 hours, Ni(II) ions hosted within the framework were exchanged for hydrated Ba(II) ions. Using X-ray crystallography and theoretical calculations the authors identified that the hydrated barium cations act as preferential adsorption sites for SO_2. Then, Chen *et al.*[142] observed high SO_2/CO_2 selectivity (325) and ultrahigh selectivities for SO_2/N_2 ($>1.0 \times 10^4$) and SO_2/CH_4 ($>1.0 \times 10^4$) in M-gallate MOFs, which was attributed to particularly favourable pore apertures and chemical functionality. In a similar vein, excellent SO_2/CO_2 selectivities have been achieved by optimising the pore aperture to approximate the size of SO_2. For instance, by modulating methyl group densities at the benzenedicarboxylate linker in $[Ni_2(BDC\text{-}X)_2DABCO]$ (BDC-X = mono-, di-, and tetramethyl-1,4-benzenedicarboxylate/terephthalate; DABCO = 1,4-diazabicyclo[2,2,2]octane) the pore size can be precisely tuned.[143] Indeed, the highly selective SO_2 adsorption by these methyl-functionalized DMOFs was accredited to the numerous non-covalent interactions between the small methyl-functionalized pore and SO_2 molecules, which was revealed by DFT calculations (this work is described in further detail below). This strategy was also investigated in ECUT-77, a Co(II)-based MOF composed of 4-(4*H*-1,2,4-triazol-4-yl)benzoate linkers, which exhibits a SO_2/CO_2 selectivity of 44 due to its small pore aperture (approximately 3 Å).[144]

Thus, as outlined above, by tuning the MOF pore aperture and allocating appropriate chemical functionality to the molecular components,[145] high SO_2 selectivities can be achieved.[146] Indeed, SO_2 adsorption based applications benefit significantly from the modular and chemically mutable nature of MOFs.[147]

2.3 Low-pressure capture of SO_2 in MOFs

Considering that concentration intervals for SO_2 detection are at the ppm level (or sometimes even the ppb level depending on the application), it is SO_2 adsorption in the low-partial pressure range that is of interest. Thus, total SO_2 uptake at ambient pressure becomes irrelevant. Instead, the most important metric for MOFs intended for SO_2 detection applications is SO_2 adsorption capacity at low pressure ($p \ll 0.1$ bar). For example, after scrubbing, SO_2 concentrations in flu gas lie between 150–450 ppm, corresponding to a shallow partial pressure (0.0005 bar)[148] and trace concentrations in the atmosphere can be considered to be under 1000 ppm. That is, SO_2 exerts a partial pressure of around 0.001 bar.[149] Ideally, a MOF should exhibit high SO_2 adsorption and affinity in a pressure range from 0.001 to 0.05 bar to be considered a candidate for SO_2 detection. Furthermore, high selectivity towards SO_2 over other atmospheric gases such as O_2, NO_x, CH_4, and CO_2 is vital. This low-pressure range could be ideal for SO_2 detection since only a few SO_2 molecules interact with the adsorption sites within the material.[60]

Some specific factors which influence SO_2 uptake in MOFs at low pressure include the SO_2 interaction mechanism and affinity (as described above) and the physical properties of MOFs, particularly the pore diameter. Indeed, the pore limiting diameter (PLD), the smallest diameter of a pore or window present in a framework, pore volume, and chemical functionalization thereof can directly influence the low-pressure SO_2 adsorption capacity. These effects can be elucidated experimentally by comparing the adsorption behavior of MOFs with diverse physicochemical properties.

In a comparative study the MOF-based (NH_2-MIL-101(Cr), Basolite F300(Fe-1,3,5-BTC), HKUST-1, ZIF-8 and ZIF-67) non-MOF-based adsorbents (Zeolite Y, SAPO-34, silica gel 60 and CTF-1, and Basolite F300) were investigated on account of their small pore diameters.[140] The prototypical MOFs listed above possess a robust structure and high chemical stability, which make them feasible for real-world applications, including gas adsorption/detection. However, ZIF-8 and ZIF-67 show low SO_2 adsorption capacity under the same conditions, which was attributed to their pore window diameter (3.4 Å) being smaller than the kinetic diameter of SO_2 (4.1 Å).[140] Thus, below the gate-opening pressure (0.3 bar), SO_2 cannot enter the pore, which significantly retards the low-pressure adsorption capacity. At 0.01 bar, the highest uptakes were 5.0 mmol g^{-1} for Zeolite Y, 2.2 mmol g^{-1} for CTF-1(400), 2.0 mmol g^{-1} for HKUST-1, and 1.9 mmol g^{-1} for SAPO-34. HKUST-1 displays the highest SO_2 adsorption at 0.1 bar among these materials (10.1 mmol g^{-1} at 293 K).[140] The outstanding performance of HKUST-1 is attributed to the presence of open metal sites in combination with an optimal PLD (5–11 Å).[123,150] The highest affinity towards and uptake of SO_2 at low partial pressures (0.01–0.1 bar) were registered for materials featuring pore diameters of ≈4–8 Å (Fig. 6) and aromatic nitrogen atoms (*i.e.*, CTF frameworks).[140]

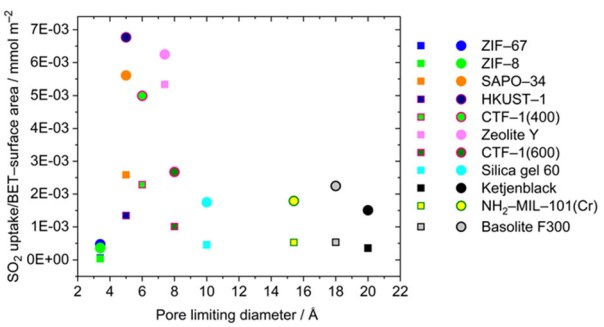

Fig. 6 Surface specific SO_2 at 0.01 bar (squares) and 0.1 bar (circles) *vs.* the pore limiting diameter. For silica gel 60, CTF-1, and Ketjenblack, only the smallest pore diameter is indicated, and these materials have a broad pore size distribution. (Reprinted with permission from the author of ref. 140 Copyright (2021) John Wiley & Sons under the Creative Commons CC-BY-NC-ND license).

Dispersion forces between a gas molecule and the pore surface are optimized when the pore diameter (defined by the Connolly surface, which is the accessible surface for a probe molecule of given size) approximates the length of the gas molecule. As alluded to above, an optimal pore aperture for SO_2 at low pressure is in a range from ≈4–8 Å. The upper limit of this range (∼8 Å = 2 × 4 Å) is approximately double the length of an SO_2 molecule and arises due to favorable dipole–dipole interactions between two SO_2 molecules bound to adjacent pore walls.[151]

Data presented in Table 1 substantiates these points. These findings support the prioritization of frameworks that feature an optimal PLD (4–8 Å), which can significantly improve SO_2 uptake at low pressure range pertinent to detection applications.

The family of isostructural M-gallate MOFs (M = Mg, Co, and Ni) exhibit record SO_2 adsorption at low pressure (0.002 bar).[142] The pore structure within these MOFs displays three-dimensional interconnected zigzag channels with a size again approximating the kinetic diameter of SO_2 (Fig. 7a–g), leading to solid confinement of SO_2. The Co, Mg, and Ni derivatives exhibit SO_2 adsorption capacities of 3.99, 4.65, and 2.67 mmol g^{-1}, respectively, at 0.002 bar and 298 K. DFT calculations indicate that the synergistic combination of hydrogen bonding interactions involving SO_2 and the unique microstructure of the MOF pores directly contribute to the high SO_2 uptake observed at low pressure.

Based on the idea that an ideal PLD can significantly enhance low-pressure SO_2 capture, the pore environment of a Ni(II)-based MOF, Ni_2(BDC-X)$_2$DABCO (X = mono-, di- and tetramethyl) was systematically modified *via* methylation to modulate the low-pressure SO_2 adsorption properties (Fig. 8).[143] In this case, four homologous MOFs were compared, where different methyl functionalization was introduced: the parent MOF (DMOF) as well as reticular frameworks composed of BDC based linkers substituted with one (M), two (DM) or four (TM) methyl groups. The BDC-TM framework (DMOF-TM) displayed the greatest low pressure SO_2 uptake (3.79 mmol g^{-1} at 293 K and 0.01 bar). This was attributed to increased steric hindrance and hydrophobicity arising from the extensive methyl substitution, leading to changes in the physicochemical properties of the framework, particularly the pore aperture.[143] Notably, the SO_2 capacity at 0.97 bar decreased with greater methyl substitution due to the systematic decrease in pore volume and BET (Brunauer–Emmett–Teller) surface area. The excellent low-pressure SO_2 adsorption capacity conforms to the expected relationship between PLD and low-pressure adsorption capacity since DMOF-TM exhibits a PLD value of ≈4.5 Å (close to the kinetic diameter of SO_2) and high uptake at low pressure (in contrast to the other methyl-DMOFs). When confined within pores that approximate the SO_2 kinetic diameter, the SO_2 molecules engage in extensive dispersion interactions with the pore surface, leading to enhanced uptake.[187,188]

2.4 Relationship between low and high-pressure SO_2 adsorption and in the textual properties of MOFs

As mentioned above, different framework properties influence SO_2 capture at low and high pressures. The results described so far indicate that BET surface area and the pore volume are the main factors contributing to high SO_2 adsorption capacity at high pressure. Fig. 9 presents the relationship between BET surface area (Fig. 9a) and pore volume (Fig. 9b) with total SO_2 uptake at 1 bar. The data indicates that MOF-808, MIL-100(Al), and NH_2-MIL-101(Al) display high SO_2 uptakes in this pressure regime due to their high surface areas. This effect is related to their micro and mesopore distribution, which improves the SO_2 uptake for MIL-100(Al) and NH_2-MIL-101(Al), associated with the large BET surface area.[151] The framework NU-1000 exhibits a mixture of micro and mesopores (∼12 and ∼29 Å) and is an outlier in the surface area/pore volume relationship observed in other frameworks (Fig. 9b). It is known that saturation is not achieved under these experimental conditions (at 1 bar and room temperature).[154] The pore volume represents a limit for the maximum SO_2 capacity for a MOF.[189] Zr-fum and NH_2-MIL-53(Al) show a low SO_2 uptake associated with the low surface area and pore volume. These results clearly illustrate the effect of surface area and pore volume on SO_2 uptake at higher pressures.

However, unlike high-pressure SO_2 adsorption, SO_2 uptake within the low-pressure range is unrelated to surface area and pore volume. Instead, the uptake at low pressure correlates with the affinity between SO_2 and the MOF pore surface. This can be mediated by chemical functionalization and/or by tuning the pore diameter using reticular synthesis techniques. Pore diameters only slightly larger than the 4.1 Å kinetic diameter of the SO_2 molecule afford high-affinity interactions at low pressure. A clear correlation can be observed by plotting the surface-specific uptake at 0.1 bar divided by the BET surface area against PLD (Fig. 9c).[190] As discussed above, pore diameter in the ∼4 and 8 Å range is optimal for high SO_2 uptake at low pressure, which correlates well with the SO_2 kinetic diameter (4.1 Å) and is supported by GCMC simulations. A PLD size within this range optimizes dispersive interactions between adsorbed SO_2 molecule and the pore surface.

To supplement this discussion, SO_2 adsorption capacities at pressure increments between 0.01 and 1 bar are summarized in Table 1 in conjunction with crucial framework metrics, including surface area, pore diameter, and pore volume. As expected from the points elaborated on above, this data confirms a relationship between the physical metrics of MOF pores and the observed SO_2 uptake. For example, as the BET surface area (Fig. 10a) and pore volume (Fig. 10b) increase, so does SO_2 adsorption capacity at 1 bar. For instance, MFM-101 exhibits a high BET surface area (2300 m^2 g^{-1}) and an outstanding adsorption capacity (18.7 mmol g^{-1}) at 1 bar and 298 K.[129] UR3-MIL-101(Cr) shows a BET surface area of 1900 m^2 g^{-1} and SO_2 capture of 13.9 mmol g^{-1} at 1 bar and 293 K.[158] MFM-422 shows a BET surface area of 3296 m^2 g^{-1} and SO_2 capture of 13.6 mmol g^{-1} at 1 bar and 298 K.[171] Ni(BDC)(TED)$_{0.5}$ displays a BET surface area of 1783 m^2 g^{-1} and SO_2 capture of 9.97 mmol g^{-1} at 1 bar and 293 K.[183] In the case of pore volume, CB6@MIL-101-Cl displays a high pore volume of 1.0 cm^3 g^{-1} with the uptake of 17.0 mmol g^{-1} at 1 bar and 298 K.[157] MIL-53(Al) with a high volume of 0.706 cm^3 g^{-1} and uptake of 10.5 mmol g^{-1} at 1 bar, and

Table 1 Comparison of SO_2 adsorption in MOFs

Material	BET SA ($m^2\ g^{-1}$)	V_p ($cm^3\ g^{-1}$)	Pore diameter (Å)	SO_2 uptake (mmol g^{-1}) at different pressure (bar) 0.01	0.05	0.1	1	T (K)	Ref.
NH_2-MIL-101(Cr)	2290	1.16	15.4	1.2	2.9$^+$	4.1	16.7	293	140
Fe(BTC)	1070	0.49	18	0.6	1.5$^+$	2.4	9.5	293	
ZIF-8	1820	0.80	3.4	0.1	0.4$^+$	0.7	8.2	293	
ZIF-67	1980	0.69	3.4	0.1	0.5$^+$	0.9	11.0	293	
HKUST-1	1490	0.61	5	2.0	7.2$^+$	10.1	13.8	293	
HKUST-1	1400					3.86	8.4	298	152
$YIL_{0.5}$@HKUST-1						5.10	7.54	298	
$PIL_{0.5}$@HKUST-1						5.15	7.73	298	
$HIL_{0.5}$@HKUST-1						5.45	8.06	298	
HIL_1@HKUST-1	600					5.71	8.33	298	
MOF-177	4100	1.51	10.6	0.3	0.5$^+$	1.0	25.7*	293	121
NH_2-MIL-125(Ti)	1560	0.651	5	3.0	4.95$^+$	7.9	10.8	293	
MIL-160	1170	0.460	5	4.2	4.8$^+$	5.5	7.2	293	
Zr-Fum	600	0.290	4.8	1.2	2.4$^+$	3.1	4.9	293	151
MOF-808	1990	0.749	4.8	2.1	2.9$^+$	3.6	14.6	293	
DUT-67(Zr)	1260	0.544	8.8	0.7	1.55$^+$	2.3	9.0	293	
NH_2-MIL-53(Al)	620	0.358	7.3	2.0	3.7$^+$	4.3	8.0	293	
Al-Fum	970	0.447	5.8	1.0	3.1$^+$	4.1	7.5	293	
CAU-10-H	600	0.258	6	1.2	3.1$^+$	3.7	4.8	293	
MIL-96(Al)	530	0.237		1.2	2.2$^+$	3.7	6.5	293	
MIL-100(Al)	1890	0.824	25	0.4	1.4$^+$	2.5	16.3	293	
NH_2-MIL-101(Al)	1770	1.001	25	1.5	2.7$^+$	3.6	17.3	293	
NU-1000	1740	1.196	12	0.6	1.5$^+$	2.6	12.2	293	
NU-1000	1970					2.1	10.9	298	153
[Ir]@NU-1000.	1842					2.4	10.6	298	
[RuGa]@NU-1000	1796			0.5		2.2	7.5	298	154
MIL-53(Al)-BDC	1450	0.706	8.5	0.4	2.45$^+$	3.3	10.5	293	151
MIL-53(Al)-BDC	1210	0.51	8.5		0.65	0.95	10.8	298	118
MIL-53(Al)-TDC	1000	0.415	8	0.6	3.6$^+$	5.0	6.9	293	151
MIL-53(Al)-TDC	1260	0.45	8		4.7		8.9	298	118
DUT-67-HCl	1349	0.509	6			3.0$^+$	9.3	298	155
DMOF	1956	0.76	7	0.25	0.9$^+$	7.21	13.09	293	143
DMOF-M	1557	0.63	7	0.46	1.8$^+$	6.40	12.15	293	
DMOF-DM	1343	0.52	7	1.0	3.0$^+$	5.70	10.40	293	
DMOF-TM	900	0.43	6	3.79	5.1$^+$	6.43	9.68	293	
HHU-2-Cl	852	0.41		2.9$^+$	3.6$^+$	4.5$^+$	9.69	293	136
HHU-2-Br	620	0.31		1.7$^+$	2.3$^+$	3.0$^+$	6.07	293	
MOF-801	939	0.43		2.1$^+$	2.9$^+$	3.9$^+$	8.00	293	
nanoCB6-H	441	0.22	6	2.3$^+$	2.9$^+$	3.4$^+$	4.98	293	156
MIL-101	3217	1.54	29	0.6	1.5$^+$	4.4$^+$	24.4	298	157
CB6@MIL-101-Cl	2077	1.0		2.0	3.0$^+$	5.2$^+$	17.0	298	
UR1-MIL-101(Cr)	1700	0.98		0.9$^+$	1.8$^+$	2.7$^+$	8.2	293	158
UR2-MIL-101(Cr)	1360	0.82		1.3$^+$	1.7$^+$	2.4$^+$	6.9	293	
UR3-MIL-101(Cr)	1900	0.96		1.8$^+$	2.9$^+$	4.0$^+$	13.9	293	
UR4-MIL-101(Cr)	1340	0.68		1.3$^+$	2.4$^+$	3.3$^+$	11.0	293	
CAU-23	1176	0.51	7.6	0.9$^+$	4.5$^+$	6.0$^+$	8.4	293	122
CCIQS-1	398		4.2				1.3	298	159
Bz@InOF-1						5.4	6.3	298	160
CAU-10	630	0.25	7			3.9	4.47	298	161
Co-URJC-5	233		8.9		0.8		1.48*	298	162
DUT-4	1348	0.71	8		2.4	5.1	13.6	298	119
SU-101	412		6.8				2.2	298	163
MFM-300(Sc)	1360	0.56	8.1		7.0		9.4	298	116
UNAM-1	522		7.3		1.1		3.5	298	164
MIL-101(Cr)-4F(1%)	2176	1.19				4.6	18.4	298	130
NiBDP	1220		9	1.52			8.48	298	165
IL/MIL-0.7	3	0.14		1.68		4.87	13.17	298	166
HBU-23	384.2		6.8				2.42	298	167
HBU-20	1551.1		7.0				6.71	298	145
ECUT-100	688	0.27	5.5				4.95	298	168
DUT-5	1611	0.9	11		2.17			298	169
PCN-250 (Fe)	1495	0.48				7.93	11.21	298	170
PCN-250 (Fe_2Co)	1583	0.51				8.06	11.92	298	
PCN-250 (Fe_2Ni)	1619	0.52				8.64	12.44	298	
PCN-250 (Fe_2Mn)	1483	0.47				7.70	11.14	298	
PCN-250 (Fe_2Zn)	1560	0.50				8.21	12.11	298	
Zr-bptc	960	0.34	4.5	2.5$^+$	5.1$^+$	6.2	7.8	298	171
UiO-66-Cu(II)	1068	0.54	7.3	0.6$^+$	2.1$^+$	3.0	8.2	298	
UiO-66-NH_2	1037	0.52	7.3	0.8$^+$	2.9$^+$	3.7	8.8	298	

Table 1 (*continued*)

Material	BET SA ($m^2\ g^{-1}$)	V_p ($cm^3\ g^{-1}$)	Pore diameter (Å)	SO_2 uptake (mmol g^{-1}) at different pressure (bar) 0.01	0.05	0.1	1	T (K)	Ref.
Zr-DMTDC	1345	0.68	7.3	0.8^+	2.4^+	3.1	9.6	298	
UiO-66	1221	0.55	7.3	0.3^+	1.7^+	2.1	8.6	298	
MFM-133	2156	0.96	10.4	0.1^+	0.8^+	1.2	8.9	298	
MFM-422	3296		7.7	0.2^+	1.0^+	1.8	13.6	298	
MFM-190(F)	2538	1.041	11	1.6^+	3.4^+	6.0^+	18.3	298	129
MFM-190(NO_2)	2304	0.962	11	1.8^+	7.1^+	10.0^+	12.7	298	
MFM-190(CH_3)	2550	1.011	11	0.6^+	3.1^+	6.9^+	15.9*	298	
MFM-100	1445	0.68	6	1.0^+	2.8^+	4.5^+	7.6*	298	
MFM-101	2300	0.885	11	2.4^+	3.1^+	8.1^+	18.7	298	
MFM-102	2873	1.138	15	1.0^+	2.2^+	3.8^+	12.1*	298	
MFM-126	965	0.47	12	2.0^+	4.8^+	5.3^+	7.3	298	
MFM-300(Cr)	1360					7.0	7.9	298	172
MFM-300($Al_{0.67}Cr_{0.33}$)	1305					8.5	9.5	298	
MFM-170	2408	0.87	15.9		4.9^+	6.2^+	17.5	298	128
MFM-305	779	0.373	6.2				6.99	298	173
MFM-305-CH_3	256	0.181	5.2				5.16	298	
MFM-600	2281		9			3.0	5.0	298	139
MFM-601	3644		12			7.9	12.3	298	
MFM-300(In)	1071	0.419	7.5		5.9	7.1^+	8.28	298	117
MFM-300(Al)	1370	0.375	6.5	4.65		7.03	7.69	293	114
Ni-gallate	455	0.154	4.85	3.37		3.79	4.49	298	142
Co-gallate	494	0.186	4.85	4.16		4.51	5.30	298	
Mg-gallate	576	0.213	4.85	4.87		5.19	5.81	298	
SIFSIX-1-Cu	1178		8.0	3.43		8.74	11.1	298	174
SIFSIX-2-Cu-i	503		5.2	4.16		6.01	6.90	298	
SIFSIX-3-Zn	250		4.2	1.68		1.89	2.10	298	
SIFSIX-3-Ni	368		4.2	2.43		2.55	2.74	298	
SNFSIX-Cu-TPA	1169			3.33			8.09	298	175
MAF-66	1226					6		308	176
F-Ce-MOF-SC-18.1@1.0PA	52.1	0.11				8.9	15.3	298	177
NbOFFIVECu-TPA	1179	0.50		2.0		3.8	6.3	298	178
TaOFFIVECu-TPA	1041	0.43		1.43		3.5	6.0	298	
ELM-12	706	0.26	4.3	0.72		1.95	2.73	298	146
CPL-1	335	0.125	4.1	0.47		1.06	2.0	298	179
Zr-TPA-HAc	2150						19.6	298	180
Zr-TPA-FA	2190						22.7	298	
men-MIL-101(Cr)	2377	1.2	2.1	3.0				298	181
18-UiO-66-cyanoacetic acid	1375	0.76					11.91	298	182
Ni(BDC)(TED)$_{0.5}$	1783	0.74	7.8			4.54	9.97	298	183
Zn(BDC)(TED)$_{0.5}$	1888	0.84	7.8				4.41	298	
DZU-17	1307.9	0.68	4				14.11	298	184
Co_6-MOF-3	1905.4	0.99	5				16.40	298	
CPL-11	1182		6.7				5.29	298	185
BUT-78	2031		15				13.8	298	186

BET SA: BET surface area, V_p: pore volume, T: temperature, $^+$taken from isotherm *structure collapse after SO_2 uptake.

293 K.[151] DUT-4 shows a high pore volume of 0.71 $cm^3\ g^{-1}$ with the uptake of 13.6 mmol g^{-1} at 1 bar and 298 K.[119] MFM-133 shows a high pore volume of 0.96 $cm^3\ g^{-1}$ with an uptake of 8.9 mmol g^{-1} at 1 bar and 298 K.[171]

We note that for studies whose sole ambition is to contend the MOF SO_2 adsorption record, a high BET surface area and high pore volume is optimal. However, such characteristics are largely irrelevant to detecting low concentrations of SO_2. Instead, selectivity and adsorption capacity at low pressure must be prioritised.

When optimizing the low-pressure SO_2 adsorption capacity, the pore diameter becomes arguably the most essential property of MOF. At 0.01 bar, high SO_2 adsorption (3–5 mmol g^{-1}) is strongly correlated to a pore diameter between 4 to 10 Å (Fig. 11), which is in good agreement with the above discussion. For example, SIFSIX-2-Cu-I with the linker 4,4′-dipyridylacetylene possesses a narrow pore diameter (5.2 Å) and a high SO_2 adsorption (4.16 mmol g^{-1}) at 0.01 bar and 298 K.[174] This is because the kinetic diameter of the SO_2 molecule (4.1 Å) is close to the pore diameter, thereby maximizing dispersion forces between SO_2 and the pore walls. In the case of SO_2 adsorption experiments, to increase the intermolecular interactions, the adequate diffusion of the SO_2 gas through the MOF pores is necessary to achieve adsorption successfully.[191]

3. MOFs applied in SO_2 detection

Although the detection of SO_2 using MOFs remains poorly explored, various techniques that leverage the advantageous features of MOFs are currently under investigation for this purpose. In principle, the presence of an analyte can be

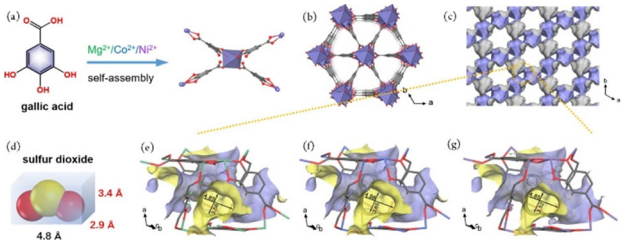

Fig. 7 (a) Illustration of the preparation process and local coordination environments of metal atoms and the ligands. (b) The structure along the *c* axis displaying the main channels and the periodic branched channels leaning against the main channels. (c) Accessible Connolly surface determined by using a probe with a radius of 1.0 Å. (d) Molecular size of the sulfur dioxide molecule. (e) 3.58 × 4.85 Å^2 for Mg-gallate, (f) 3.68 × 4.95 Å^2 for Co-gallate, and (g) 3.52 × 4.85 Å^2. (Reprinted with permission from ref. 142 Copyright (2021) American Chemical Society).

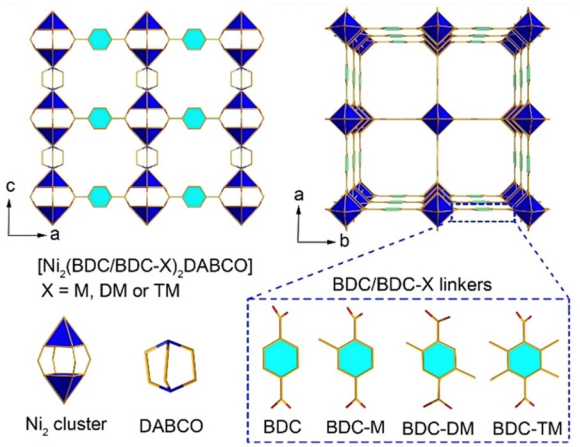

Fig. 8 Top row: Sections of the packing diagram of DMOF showing the channel structures along the *b*- (and identical *a*-) axis and along the *c*-axis. Bottom row: The building blocks of the Ni_2 cluster, DABCO, and BDC/BDC-X in DMOF/DMOF-X. X represents the monomethyl (M), 2,5 dimethyl (DM), or 2,3,5,6 tetramethyl (TM) substituents. (Reprinted from ref. 143 Copyright 2021 with permission from John Wiley & Sons under the Creative Commons CC-BY-NC-ND license).

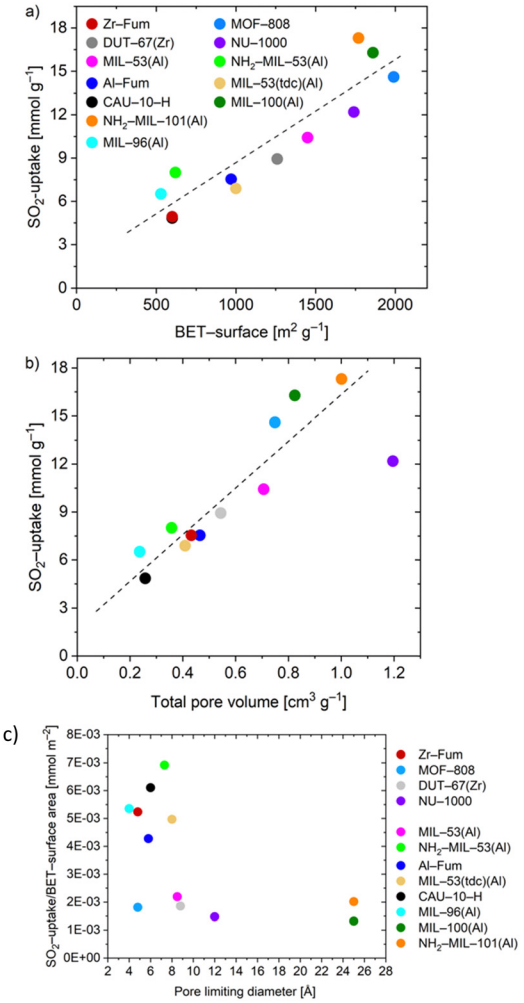

Fig. 9 SO_2 uptake (1 bar, 293 K) *vs.* (a) BET-surface area and (b) total pore volume. The dashed line is a trend line as a guide to the eye, (c) surface-specific SO_2 uptake at 0.1 bar (293 K), which is the uptake at this pressure divided by the BET-surface area *vs.* the pore limiting diameter (PLD). (Reprinted with permission from ref. 151 Copyright (2021) American Chemical Society).

confirmed by monitoring characteristic MOF properties that are altered after an external stimulus (in this case, the SO_2 interaction). This is the fundamental principle upon which MOF-based sensors are premised. The response to the host–guest interaction provides a probe for qualitative and quantitative sensing or detection applications. Only a few MOFs have been employed for SO_2 detection and these have been based on (i) analyte-induced changes in their luminescent properties (generating an energy transfer), (ii) changes in the electrochemical properties (changes in electrical resistance), (iii) changes in spin-crossover (SCO) behavior (change in the spin state), and (iv) a change in the sample mass. To supplement this discussion, the MOF-based materials applied for SO_2 detection are summarized in Table 2 in conjunction with crucial parameters, including sensing technique, sensitivity, and selectivity.

3.1 MOFs for luminescent SO_2 detection

Luminescence behavior has been extensively studied in the MOF field.[215] Generally, such materials are called luminescent metal–organic frameworks (LMOFs) and have been used in optical, medical, and detection applications.[216–218] Different strategies have been developed to construct luminescent MOFs, which are based on the "signal-off" or "signal-on" response strategies (in other words, the so-called turn-on and turn-off effect).[219] The emission centers in such materials may constitute the metal ions, organic linkers, and guest species. The organic linkers typically present π-conjugated systems, facilitating a fluorescence response due to accessible π–π* transitions.[220] In the case of metal centers, the lanthanide family – particularly Tb^{3+} and Eu^{3+} – are frequently employed due to the accessible transitions between $^5D_0$–^7F_j states.[221] Considering these properties, MOFs are excellent candidates for the detection of not only SO_2 but also multiple analytes

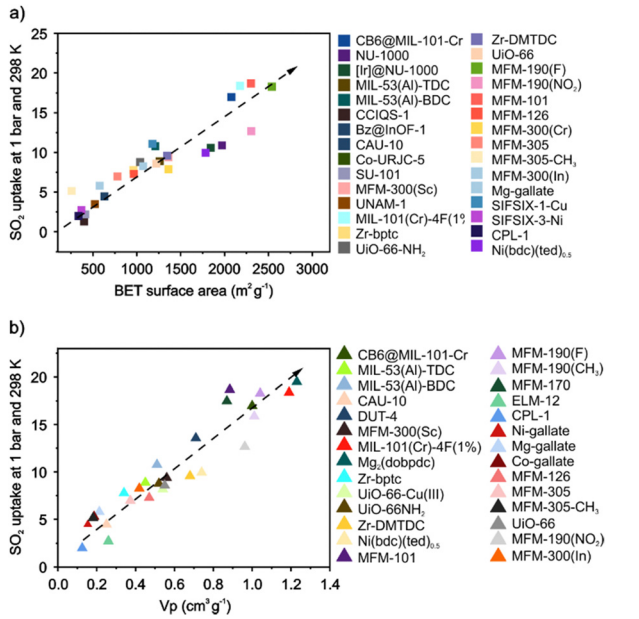

Fig. 10 Relation between SO_2 uptake at 1 bar and 298 K and (a) BET surface area and (b) pore volume. For references to the individual MOFs, see Table 1.

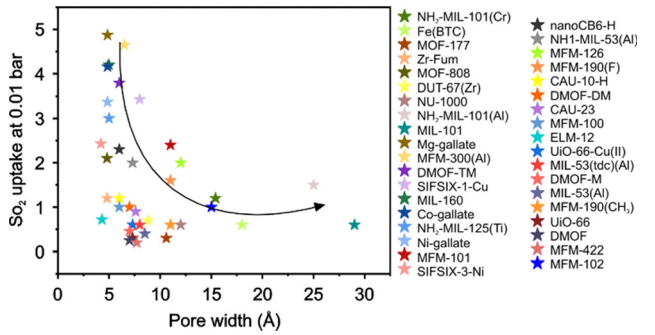

Fig. 11 Relation between SO_2 uptake at 0.01 bar with PLD. For references to the individual MOFs, see Table 1.

using luminescent properties.[96] Notably, the rational construction of LMOFs that exhibit energy transfer properties can tune the luminescence.[222,223]

LMOFs can be synthesized with a tremendous diversity of organic linkers and metal clusters (including pristine MOFs or with linker modifications), providing a wide range of energy transfer LMOFs (ET-LMOFs),[224] affording multiple detection options depending on the target analyte.[225] Additionally, chromophores can be regularly aligned and carefully ordered inside the crystalline LMOF lattice, providing a basis for understanding the short- and long-distance energy transfer mechanisms.[226] The high crystallinity and periodicity of MOFs are advantageous for computational models and calculations that aim to elucidate the luminescence mechanism of LMOFs.[227,228]

LMOFs have been intensely studied for solar cells,[229] photocatalysis,[230] scintillators,[231] X-ray and NMR imaging,[232] and for detecting analytes pertinent to gas pollution.[84] The possible luminescent centers and charge transfer processes in LMOFs (Fig. 12) are classified as (Fig. 12a) linker-centered emission, guest-centered emission, and metal-centered emission, and (Fig. 12b) linker-to-linker, metal-to-metal, metal-to-linker, the linker-to-metal, guest to host, and host to guest.[233] Herein, we will not specifically discuss each case since this would constitute a significant departure from the stated aim of this contribution. However, we provide a brief description when necessary and encourage readers to consider several relevant contributions.[234,235] Aside from possessing suitable luminescent behavior, the first essential requirement for an LMOF to be considered for SO_2 detection applications is demonstrable chemical stability towards SO_2 under ambient conditions (including humidity), as previously mentioned (*vide supra*).

For example, Chen and Wang reported a Ce^{4+}/Tb^{3+} MOF, Ce–PA–Tb MOF, with the linker PA = *m*-phthalate, with promising attributes for SO_2 detection.[195] The design of this novel MOF was inspired by the advantages of lanthanide luminescent properties, which include a long luminescence lifetime.[236] The MOF is a bimetallic material with Ce^{4+} and Tb^{3+} centers coordinated with PA linkers. To assess the detection prowess of the material, the authors generated SO_2 gas *in situ* using 'Kipp's device' – a chamber wherein sodium sulfite (Na_2SO_3) is combined with sulfuric acid (H_2SO_4) under a N_2 atmosphere to generate the SO_2 gas (Fig. 13). Samples containing SO_2 were analyzed using three separate methods: Ce–PA–Tb MOF probed by luminescence, Ce–PA–Tb MOF incorporated into a test strip, and formaldehyde absorbing pararosaniline spectrophotometry (FAPA). The limit of detection (LOD) was found to be 0.006 μg mL^{-1} (0.093 μM), 0.5 μg mL^{-1} (7.8 μM), and 0.05 μg mL^{-1} (0.78 μM) for the respective detection methods. Notably, the luminescence-based measurement is ten times more sensitive to SO_2 than the Ce–PA–Tb-MOF test strip method or FAPA. The mechanism involves the SO_2-induced reduction of Ce^{4+} to Ce^{3+}; subsequent irradiation with 250 nm photons induces an energy transfer from Ce^{3+} to the adjacent Tb^{3+} ion. An electronic transition within the Tb^{3+} ion leads to emission at 545 nm, which is measured. Crucially, the energy transfer does not occur from Ce^{4+} to Tb^{3+}. The presence of Ce^{3+} was confirmed using XPS spectroscopy. It was not stated if the sensor is re-usable.

The use of luminescent MOF-based SO_2 sensors was recently expanded with the development of a DNA-based Tb-MOF composite for SO_2 detection.[196] Briefly, single-stranded DNA (ssDNA) was combined with Tb^{3+} to form ssDNA-Tb^{3+} which was combined with IR-MOF-3 MOF in an ethanol suspension to form a composite. A test strip was fabricated using the DNA-based Tb-MOF composite in this case. The authors used Kipp's device to generate SO_2 for the purpose of assessing the performance of the composite sensor. The results indicate a LOD value of 0.02 ppm of SO_2, a low value which confirms that the material provides a promising platform for SO_2 detection. The DNA-based Tb-MOF composite exhibits a weak PL emission and displays an apparent turn-on effect after interaction with SO_2 and analogues thereof. The authors suggested that the material operates *via* a charge transfer mechanism: the amino

Table 2 Comparison of SO_2 detection in MOFs

Material	Method	Matrix	Selectivity	SO_2 concentration range	SO_2 detection level	Mechanism	Ref.
Eu-BDC-NH_2 film	Luminescence	MOF film	Over N_2, CO_2, O_2, NH_3, HCHO, H_2O, and H_2S	0–200 ppm	0.65 ppm	Turn-off effect by energy transfer	192
MOF-303	Luminescence	Solid state (powder)	Over CO_2, CH_4, and H_2O	Up to 0.1 bar		Turn-on effect	193
CYCU-3	Luminescence	Solid state (powder)	Over CO_2, and H_2O	Up to 0.1 bar		Turn-on effect by energy transfer	194
Ce–PA–Tb	Luminescence	Solid state (powder)		0–70.4 ppm	0.093 μM	Turn-on effect by energy transfer	195
DNA–Tb-MOF	Luminescence	Test paper		0.2–1.6 ppm	0.02 ppm	Turn-on effect by energy transfer	196
MOP-CDC	Luminescence	Solid state (powder)		Up to 0.1 bar		Turn-off effect	197
Mg_2DOBPDC	Luminescence	Solid state (powder)		Up to 0.1 bar		Turn-on effect	198
Ni_2(dobpdc)	Luminescence	Solid state (powder)	Over CO_2, and H_2O	Up to 0.1 bar		Turn-on effect	199
MIL-53(Cr)-Br	Luminescence	Solid state (powder)	Over CO_2, and H_2O	Up to 0.1 bar		Turn-on effect	200
MUF-16	Luminescence	Solid state (powder)	Over NO_2, CO_2, H_2O, H_2S, O_2, N_2, and CH_4	Up to 0.1 bar		Turn-on effect	201
		THF suspension		1–250 mM	80.72 ppm		
MOF-5-NH_2	Luminescence	Test paper	Over NO_2, NH_3, N_2, CO_2, H_2S, and CS_2	0–3 ppm	0.05 ppm	Turn-on effect	202
UTSA-16(Zn)	Luminescence	THF suspension		1–5 mM	114.6 ppm	Turn-off effect	203
Ni_3BTC_2/OH-SWNTs	Electrochemical	Microelectrode	Over NO_2, CH_4, CO, and C_2H_2	4–20 ppm	4 ppm	Electron transfer	204
CoZn-NCNTs	Electrochemical	Solid state (powder)	Over NO_2, MeOH, acetone, NH_3, CO, H_2, and EtOH	0.5–30 ppm	0.5 ppm	Increase of hole density	205
Ni-MOF/-OH-SWNTs	Electrochemical	Solid state (powder)	Over NO_2, NH_3, and CO	0.5–15 ppm	0.5 ppm	Electron transfer	206
UiO-66-NH_2/PVDF NM	Electrochemical	Nanofibers membrane		1–150 ppm		Interaction with NH_2 groups	207
PAN@UiO-66-NH_2 NM	Electrochemical	Nanofibers membrane	Over CO, CH_4O, C_2H_6O, C_3H_8O, and C_3H_6O	1–125 ppm		Interaction with NH_2 groups	208
UiO-66-THB/PAN-based	Electrochemical	Electrode	Over CO_2, H_2S, NO_2, NO, CO, NH_3, C_3H_6O, and C_2H_6O	1–125 ppm	0.1 ppm	Hydrogen bonding	209
TM-Ag@NU-901	Electrochemical	MOF film		10–200 μM	0.1 ppm	Interaction with C=C groups	210
UiO-66-NH_2	Electrochemical	Solid state (powder)		1–10 ppm	1 ppm	Formation of a charge-transfer complex	211
MFM-300(In)	Electrochemical	Electrode	Over CH_4, H_2, CO_2, C_3H_8, C_7H_8, and NO_2	75–1000 ppb	75 ppb	Capacitance	212
Fe(PZ)[Pt(CN)$_4$]	Magnetism	Solid state (powder)	Over CO_2, and CS_2			Stabilization of the LS state	213
KAUST-7	Gravimetric	QCM	Over H_2O	0–500 ppm	5 ppm	Mass change	214

groups present in DNA–Tb-MOF function as electron-donors from the perspective of the Tb^{3+} ions. When SO_2 and its analogues such as HSO_3^- interact with the amino group, it negates the typical energy transfer between the amino group and Tb^{3+} ions, generating a PL turn-on effect at 491, 546, 585, and 620 nm upon irradiation at 290 nm. These investigations confirm that Tb-MOFs exhibit luminescent properties which form a promising basis for SO_2 detection.

Interestingly, apart from the mechanisms already discussed, changes in luminescence may also be induced by the interaction between SO_2 and the structural linkers. A Cu(II)–metal–organic polyhedron (MOP-CDC, CDC = 9*H*-carbazole-3,6-dicarboxylate) displays a turn-off effect in its fluorescence after SO_2 adsorption.[197] At low pressure (0.05 bar), MOP-CDC exhibits an SO_2 uptake of 1.0 mmol g^{-1} at 298 K. Under 440 nm excitation, MOP-CDC exhibits strong fluorescence emission at 540 and 639 nm. After the SO_2 exposure, these bands are quenched, providing a convenient probe for the presence of SO_2. DFT calculations demonstrate that the SO_2 molecule interacts with the carbazole NH site through hydrogen-bonding [N–H···O=S=O]. Due to this strong host–guest interaction, SO_2 adsorption induces fluorescence quenching. Notably, CO_2 adsorption (a potential interfering gas) had no apparent effect on fluorescence intensity.

However, in some cases, energy transfer processes involving the organic linker result in a turn-on effect. For instance, Mg_2DOBPDC (DOBPDC = 4,4-dioxidobiphenyl-3,3-dicarboxylate), which shows high SO_2 adsorption at low pressure (0.05 bar, 6 mmol g^{-1} at 298 K).[198] At an even lower pressure of 0.002 bar, the material displays an SO_2 uptake of approximately 2.4 mmol g^{-1}.

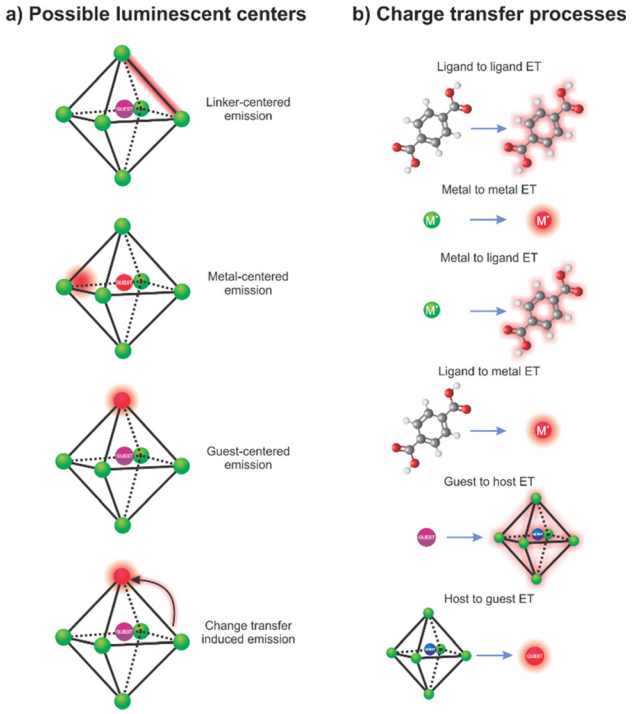

Fig. 12 Schematization of (a) possible luminesce centers and (b) charge transfer processes. Based on ref. 233.

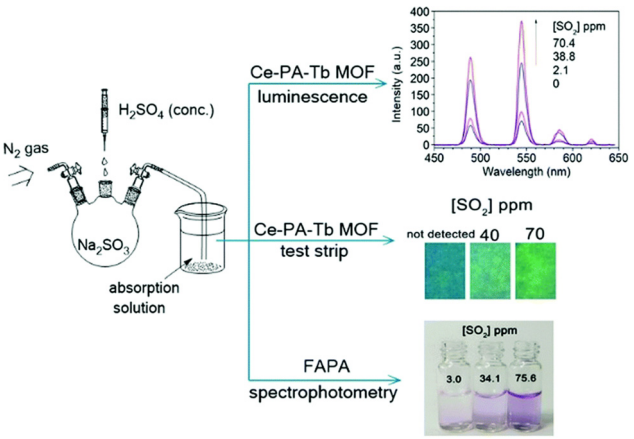

Fig. 13 Determination of SO_2 gas by the methods of standard formaldehyde absorbing pararosaniline (FAPA) spectrophotometry, Ce–PA–Tb luminescence and Ce–PA–Tb test strip with a 254 nm UV lamp. (Reprinted from ref. 195 Copyright 2020 with permission from Royal Society of Chemistry).

This value is comparable to record low pressure SO_2 adsorption exhibited by M-gallate MOFs[142] and several frameworks listed in Table 1. GCMC simulations revealed that SO_2 preferentially adsorbs at open Mg^{2+} coordination sites in a monodentate fashion (SO_2(O)–Mg = 2.17 Å). Nevertheless, the coordinated SO_2 also engages in hydrogen bonding with the adjacent DOBPDC linker, thereby modulating the luminescent properties of the material. Thus, during SO_2 exposure under 320 nm irradiation, the broad

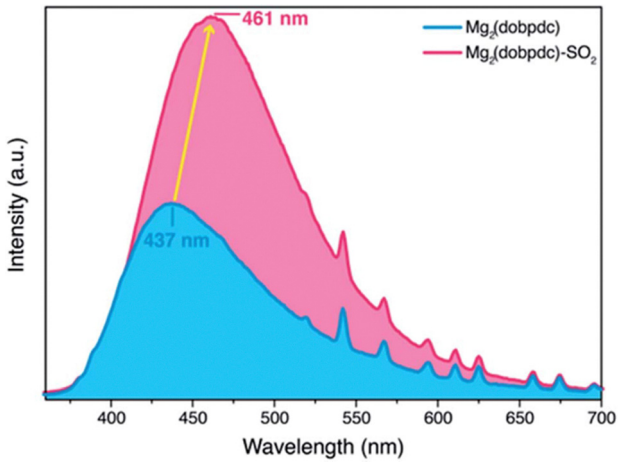

Fig. 14 Emission spectra of Mg_2(dobpdc) before (blue) and after (pink) exposure to SO_2. Both samples were excited with 320 nm UV light. (Reproduced from ref. 198 Copyright 2022 with permission from Royal Society of Chemistry).

photoluminescence band at 437 nm shifts to 461 nm, concomitantly increasing the band's intensity (Fig. 14).

In addition, the isostructural framework Ni_2(DOBPDC) was investigated for application in SO_2 detection.[199] Under 350 nm irradiation, Ni_2(DOBPDC) exhibits a broad emission band at 450 nm. After the sample is exposed to SO_2, the emission peak shifts to 405 nm with a 61% increase in emission intensity. This behavior was observed even at low SO_2 pressure (0.1 bar). To investigate the luminescent mechanism, a time-resolved photoluminescence (TRPL) experiment was performed using a 340 nm picosecond-pulsed LED as the excitation source. The results revealed that the average decay lifetime increases from 2.14 to 2.47 ns upon SO_2 exposure. This suggests that interaction between the SO_2 and Ni^{2+} centers within the framework nullifies the organic linker's molecular motion, minimizing the non-radiative decay pathways available and thereby causing the fluorescence lifetime to increase.

MOF-303 is composed of Al(III) centers which are interconnected by PZDC linkers (PZDC = 1*H*-pyrazole-3,5-dicarboxylate) and was recently evaluated for SO_2 detection.[193] MOF-303 displays one of the highest low pressure SO_2 adsorption capacities so-far reported (6.21 mmol g^{-1} at 298 K and 0.1 bar). At 298 K, the first adsorption step occurs at 0.05 bar and corresponds to 5.44 mmol g^{-1} of SO_2, confirming a high affinity between SO_2 and MOF-303. *In situ* diffuse reflectance infrared Fourier transform spectroscopy (DRIFTS) experiments revealed the preferential adsorption sites to be μ_2-OH and linker N–H sites, which interact with SO_2 through hydrogen bonding. In this material, a hydrogen-bonded dimer forms *via* adjacent pyrazole groups within the pore, generating hydrophilic pockets that bind small molecules, here SO_2. Considering the fluorescent properties of the PZDC linker in several coordination compounds, the luminescent properties of MOF-303 were investigated. However, in MOF-303, the linker fluorescence is quenched because the absorbed energy is released through non-radiative pathways. However, exposure to SO_2 under 248 nm irradiation resulted in

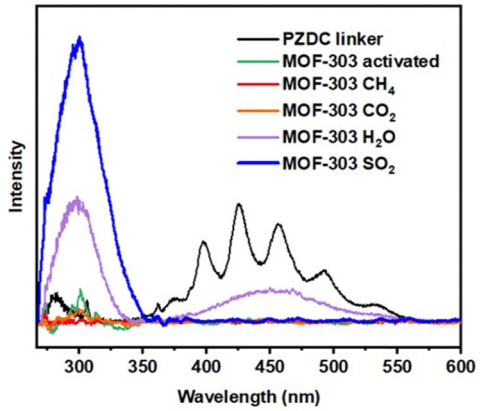

Fig. 15 Solid-state emission spectra of PZDC linker (black line), activated MOF-303 (green line), after exposure to: CH_4 (red line); CO_2 (orange line); H_2O (purple line); and SO_2 (blue line). The excitation wavelength was set at 248 nm. (Reproduced from ref. 193 Copyright 2022 with permission from American Chemical Society).

a fluorescence turn-on effect with emission at 299 nm (Fig. 15). This represents an approximately 125 nm shift in emission relative to that of the linker. No apparent change in emission was observed in the presence of the common interfering gases CH_4 or CO_2. The authors suggest that the physisorption of SO_2 within MOF-303 leads to a rigidification of the structure which suppresses non-radiative decay pathways, thereby intensifying emission.

Similarly, CYCU-3, also an Al(III)-based MOF but composed with SDC linkers (SDC = 4,4′-stilbenedicarboxylate), was assessed for SO_2 detection and capture applications.[194] CYCU-3 shows a total uptake of 11.03 mmol g^{-1} at 1 bar and 298 K. The interaction between SO_2 and the pore surface was elucidated using *in situ* DRIFTS experiments and theoretical calculations. Bridging hydroxyl moieties within the inorganic cluster were identified as preferential interaction sites for SO_2. The fluorescence spectra of both CYCU-3 and solid H_2SDC were recorded. Under 343 nm irradiation, H_2SDC produces a fluorescence emission peak at 450 nm. However, the fluorescent emission from CYCU-3 is blue shifted and less intense than that of the free ligand due to charge transfer between the organic linker and Al(III) centres. After the sample is exposed to SO_2 under irradiation at 343 nm, the emission at 450 nm increased in intensity. This performance was attributed to an enhanced ligand-centered $\pi^* \rightarrow \pi$ electronic transition.

Cr(III)-MOFs have also been applied for SO_2 adsorption and detection, including MIL-53(Cr) (linker: BDC) and the novel reticular analogs MIL-53(Cr)-Br and MIL-53(Cr)-NO_2 with the linkers BDC-Br and BDC-NO_2 respectively.[200] In the presence of SO_2, these MOFs show a turn-off effect under irradiation at 300, 360, and 350 nm, respectively, corresponding to a decrease in the emission intensity at 415, 420, and 507 nm, respectively. The intensity decrease was associated with a charge transfer process involving the organic linker. MIL-53(Cr) displays a slight red shift, suggesting metal-to-linker charge transfer while MIL-53(Cr)-Br shows a change in the emission peak from 450 to 436 nm.

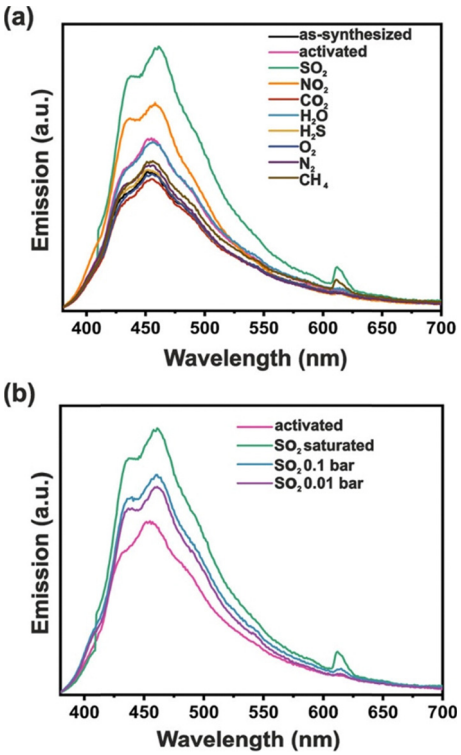

Fig. 16 (a) Comparison of solid-state emission spectra of MUF-16 exposed to different gases, and (b) comparison of solid-state emission spectra of MUF-16 exposed to different SO_2 pressures (Reproduced from ref. 201 Copyright 2024 with permission from American Chemical Society Under CC-BT 4.0 license).

MUF-16 is a Co(II) based framework composed of 5-aminoisophthalate (AIP) linkers, formula [Co(AIP)$_2$], which was explored for the selective detection and capture of SO_2.[201] The SO_2 adsorption isotherm shows an uptake of 2.2 mmol g^{-1} at 298 K and 1 bar. Employing FTIR, DFT calculations, and GCMC simulations, SO_2 was found to engage in favorable hydrogen bonding interactions with the amino groups which decorate the framework. An increased fluorescence response is observed in the presence of SO_2 compared to the other common gases such as CO_2, NO_2, N_2, O_2, CH_4, and water vapor (Fig. 16a and b). The LOD was calculated using a THF solution of SO_2 and was found to be 1.26 mM ($\sim$81 ppm). A fluorescence mechanism was proposed using TRPL analysis.[201]

The amino-functionalized derivative of MOF-5, IR-MOF-3, was incorporated into a test strip for rapid and selective sensing of SO_2 and its derivatives *via* a luminescence enhancement turn-on effect.[202] The test strip offers real-time detection of SO_2 with a detection limit of 0.05 ppm. Within IR-MOF-3 the amino groups donate electron density to the metal centres which quenches the luminescence. However, when SO_2 (or HSO_3^{2-}) interacts with the amino group, a complex is formed which disrupts the linker-to-metal charge transfer process, turning on the characteristic luminescence of the linker. XPS spectroscopy confirms the formation of N–S interactions between amino groups within IR-MOF-3 and SO_3^{2-}. Test strips containing MOF-5 and IR-MOF-3 were exposed to SO_2 gas generated using

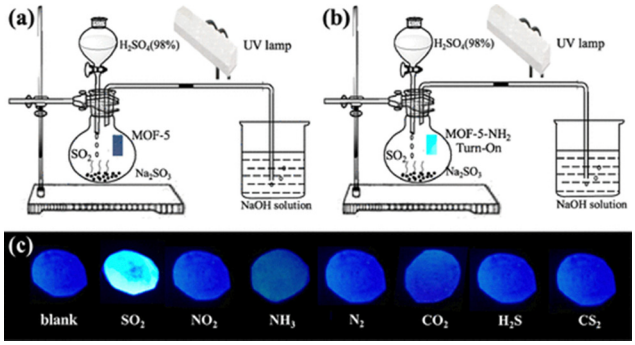

Fig. 17 (a) and (b) Schematic diagrams of the device for detecting SO_2 gas using MOF-5 and MOF-5-NH_2 luminescent test paper, respectively. (c) Luminescence response photographs of MOF-5-NH_2 luminescent test paper after exposure to various gas species under a 365 nm UV lamp. The final concentrations of SO_2, NO_2, NH_3, N_2, CO_2, and H_2S were 2 ppm, while CS_2 gas was saturated vapor of liquid-state CS_2. (Reproduced from ref. 202 Copyright 2018 with permission from American Chemical Society).

a Kipp apparatus (Fig. 17a–c). Notably, unfunctionalized MOF-5 exhibits no response to SO_2. The test strip impregnated with MOF-5-NH_2 was found to be stable after exposure to SO_2, suggesting that the system is reusable for detecting SO_2 with a particularly short 15-second response time. The LOD was calculated to be 0.05 ppm for the test paper. It is worth mentioning that the chemical stability of MOF-5 should be considered when evaluating its suitability for SO_2 detection. The material has for instance proven unstable to water.[237]

A technique, named *in situ* secondary growth, allows MOFs to be deposited on membranes. Qian *et al.*[192] reported a MOF film based on a Eu(III) MOF with BDC-NH_2 linkers. First, the authors prepared a hydroxyl functionalized glass surface using 'piranha' solution (H_2SO_4/H_2O_2 solution). Then, UiO-66-NH_2 was synthesized *in situ* on the functionalized glass. Subsequently, the Eu-MOF was grown by solvothermal synthesis to form a layer which acts as a fluorescence probe for SO_2. Exposure to SO_2 leads to quenching of the fluorescent solid emission due to the $^5D_0 \rightarrow {}^7F_2$ transition of Eu^{3+}. The decay curves for N_2 and SO_2 indicate a reduced emission lifetime of 381.8 μs in 1% SO_2, suggesting the involvement of a charge transfer process between the linker and SO_2 molecules. The LOD value was reported to be 0.65 ppm with a response time of as short as 6 s.

3.2 MOFs for electrochemical SO_2 detection

Besides the luminescence-based sensors described above, electrochemical processes have also been widely used for small molecule detection and quantification. The operation of electrochemical sensors depends on electron transfer events that occur during interactions between the surface of the material and analyte gas molecules.[238] The transfer of electrons accompanying analyte interactions leads to a change in resistance, which can be measured. This change in resistance, and therefore the sensor's sensitivity, depends to a considerable extent on the nature of the material with which the analyte interacts.[239] Materials commonly employed in electrochemical sensors include metal oxides, carbons, nitrides, sulfides, and – to a growing extent – MOFs. The most important parameters to consider in achieving optimal performance are selectivity, response and recovery speed, and stability.[240] The surface area and the reactivity of the surface towards the analyte strongly influence the response. A high response factor can be accompanied by a low LOD, the minimum analyte concentration to which the sensor is sensitive. Various interfering species may be present in the environment besides the analyte of interest. Thus, selectivity is crucial for accurate and reliable detection and is usually evaluated by cross-sensitivity comparison wherein the senor is exposed to various interfering species at fixed concentrations. Selectivity is affected by many factors related to the environment, such as humidity and temperature, the nature and composition of the sensor, the affinity between the gas molecules, and the properties of the sensor material.[241]

Electrochemical techniques are now being implemented for SO_2 detection using MOFs. For example, a composite based on nickel benzene-tricarboxylate (Ni_3BTC_2) and OH-functionalized single-walled carbon nanotubes (OH-SWNTs) was investigated for this purpose.[204] After the composite was exposed to SO_2, the measured change in voltage was successfully related to the SO_2 concentration. A response time of 4.59 s with a recovery time of 11.04 s was achieved with a low SO_2 concentration (15 ppm). This behavior was attributed to an electron transfer from the composite to the SO_2 molecule. In this case, the composite is a p-type material, where a transfer of electrons from the composite to the SO_2 molecule (an electron acceptor) occurs. The selectivity of the composite sensor is maintained in the presence of NO_2, CH_4, CO, and C_2H_2, typical interfering gases in nature.

Moreover, the relative change in electrical resistance can also be leveraged for small molecule sensing. For example, in 2018 Li *et al.*[205] reported a composite material derived from pyrolysis of Zn/Co bimetallic ZIF-67 which undergoes a 53% change in resistance in the presence of SO_2 (100 ppm). A cross-selectivity test was performed using NO_2, MeOH, acetone, NH_3, CO, H_2, and EtOH vapor. The material shows high selectivity over these gases even at low SO_2 concentrations (30 ppm). The response and recovery times are reportedly 88 and 900 s, respectively, with a limit of detection for SO_2 equal to 0.5 ppm.

The changes in the electrical resistance of a Ni-MOF composite (Ni-MOF/-OH-SWNTs) allowed a rapid response time of 10 s with a fast recovery time of 30 s for SO_2 (1 ppm).[206] This function is maintained even in the presence of NO_2, NH_3, and CO. It is known that holes form the major charge carrier within the Ni-MOF composite in the absence of SO_2. However, since SO_2 acts as an electron donor it acts to reduce the population of holes *via* recombination. Because holes are the major carrier within the composite the presence of SO_2 leads to a quantifiable increase in resistance.

Building on these developments, Zhang *et al.*[207] reported a capacitive sensor composed of UiO-66-NH_2 incorporated into a nanofiber membrane composed of polyvinylidene fluoride and carbon nanotubes. The composite material was employed as a sensing layer for real-time monitoring of SO_2. The amine

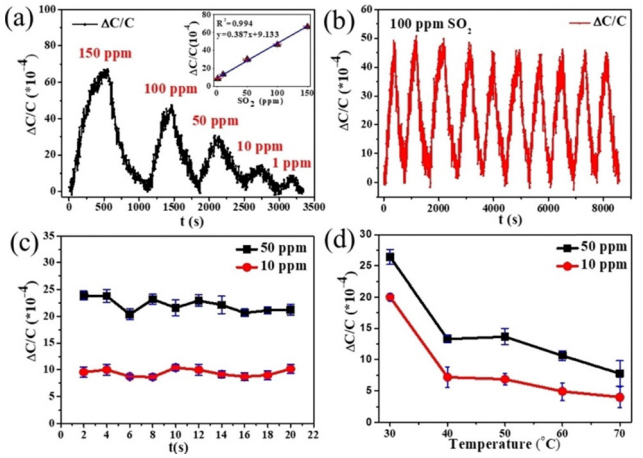

Fig. 18 (a) Detection of SO_2 in the range of 1 to 150 ppm concentration and linear response for the testing range of the inset; (b) reproducibility for the detection of 100 ppm SO_2; (c) response ability for the sensor at 10 and 50 ppm SO_2 within 20 days; (d) temperature influence on the sensor performance. (Reproduced from ref. 207 Copyright 2021 with permission from John Wiley & Sons).

functional groups interact strongly with SO_2 inside the sensor, leading to a change in conductivity (Fig. 18a–d). The detection response time was reportedly 435 s and 185 s towards 150 ppm and 1 ppm SO_2, respectively. Importantly, the SO_2 concentration and change in capacitance are strongly correlated, which was attributed to the adsorption capacity of UiO-66-NH_2. The sensor also shows high reproducibility for 100 ppm SO_2 over ten consecutive cycles. A long-term study was conducted over the course of 20 days in which 10 and 50 ppm SO_2 samples were measured, the change in conductivity was retained ~89% of its original value over this time. The SO_2 sensing performance is stable towards moderate temperature changes, dropping only 22% in going from 30 to 70 °C.

To improve the response time of the nanofiber membrane, the authors also designed a new flexible gas sensor in which UiO-66-NH_2 was incorporated into electrospun polyacrylonitrile (PAN) nanofibers.[208] The device was equipped with carbon nanotube electrodes. The high surface area and porosity of UiO-66-NH_2 make it particularly useful in an electrochemical detection device since the analyte can rapidly diffuse into the MOF. Crucially, the well-established flexibility of the membrane provides exceptional long-term stability.[242] The sensor reportedly to operates with a 1 ppm LOD for SO_2, and the porous MOF platform facilitates rapid SO_2 diffusion within the material with a fast response time of 255 s.

In a separate investigation from the same research group, the MOF UiO-66-NH_2 was incorporated into a nanofiber membrane which was modified to improve SO_2 adsorption and thereby improve the limit of detection.[209] UiO-66-NH_2 was loaded onto a PAN nanofiber membrane and modified with 2,3,4-trihydroxybenzaldehyde (THBA). The composite was synthesized by using imine condensation to cross-link the amine and aldehyde groups to form a Schiff base and obtain a UiO-66-N═C-THB/PAN-based capacitive gas sensor. This design achieved a lower SO_2 detection limit of 0.1 ppm. Based on DFT calculations, hydrogen bonding between SO_2 and the THB hydroxyl groups resulted in a high adsorption affinity. Considering the potential of MOF-based membranes in SO_2 detection applications, NU-901 (with the linker TBAPy = 4,4′,4″,4‴-(pyrene-1,3,6,8-tetrayl)tetrabenzoate) was embedded in a silica film.[210] This film was modified with thiol-magenta (TM) and Ag nanoparticles (TM-Ag@NU-901). SO_2 was detected by surface-enhanced Raman scattering, a new alternative strategy for detecting SO_2.

The UiO-66 analogs UiO-66-NH_2 and UiO-66-OH were employed as chemoresistive sensors for SO_2, NO_2, and CO_2.[211] Archetypal UiO-66 does not exhibit a change in resistance after exposure to any of the acidic gases listed above. However, UiO-66-NH_2 responds with a 22 ± 3% change in resistance to the presence of 10 ppm SO_2, with a 1 ppm LOD (corresponding to a 3.2 ± 0.2% response). This performance was attributed to the formation of a charge-transfer complex when SO_2 interacts with the amine-functionalized linker.

As discussed already, MFM-300(In) exhibits outstanding properties for SO_2 sorption and sensing applications due to a high SO_2 uptake at low pressure and excellent stability. Building on previous work, MFM-300(In) was applied as an electrode for SO_2 detection.[212] The In(III)-based MOF was coated on interdigitated electrodes, and the capacitance changes that occur in response to SO_2 were measured. This sensor displays one of the highest sensitivities to SO_2 and excellent selectivity over interfering gases such as methane, hydrogen, carbon dioxide, nitrogen dioxide, propane, and toluene at 1000 ppb. SO_2 concentration was successfully measured from 75 to 1000 ppb with a detection limit of 5 ppb. The electrochemical response was attributed to the interaction between SO_2 and the μ_2-OH groups in the MOF node (through hydrogen bonds), with further dipole–dipole interactions between adsorbed SO_2 molecules. The resulting electrostatic changes perturb the capacitance of the electrode.

3.3 Other detection techniques

In addition, MOFs have been employed in alternative SO_2 detection systems that use magnetic and mass change sensors. These provide an opportunity to exploit the diverse physicochemical properties of MOFs that do not find utility in the sensing techniques explored so-far. However, only a few examples have been reported, and we therefore emphasize the opportunity these methodologies present for future sensing applications.

In general, for magnetic gas sensors involve analyte-induced changes to the magnetic properties of the sensing material. Such changes can be measured through a range of sophisticated techniques that are beyond the scope of this review.[243] Magnetic gas sensors offer advantages over other gas sensors; for example, they can be designed to operate in a wide temperature range, do not require an electrical current source (therefore, the risk of explosion or fire is reduced), and the response time is much reduced compared to chemosensitivity sensors.[244,245] Various materials are employed as sensing

materials in magnetic gas sensors, recently this has included MOFs.[246,247]

Spin-crossover has emerged as an essential chemical phenomenon upon which magnetic gas sensors can be designed. Recently, MOFs that exhibit spin-crossover behavior have been studied. These typically exhibit structural nodes with $3d^4$–$3d^7$ transition metals in an octahedral coordination geometry. The spin-crossover phenomenon involves stimuli-induced switching between a low-spin and high-spin electronic configuration.[248,249] Of relevance in gas sensors, this change can be induced by the interaction between an analyte gas and the sensing material.

For example, Pham *et al.*[213] undertook a highly explorative study to demonstrate in principal that spin-crossover (SCO) behavior in a MOF can be exploited for SO_2 detection. {Fe(PZ)[Pt(CN)$_4$]} (PZ = pyrazine) was used to explore how adsorption of SO_2 affects the population of high and low spin states. Differences between the SCO properties of {Fe(PZ)[Pt(CN)$_4$]} during the adsorption of various gases point to specific guest–framework interactions, which appear to be sensitive to the physicochemical properties of the guest molecule. In this case, the gas molecules stabilized the LS state of the framework. The material was exposed to CO_2, SO_2, and CS_2 during the heating process in both experimental and simulated settings (Fig. 19). The SO_2 molecule was found to stabilize the LS state, leading to a 20 K shift in temperature caused by changes in the Fe–N bonds within the framework.

Mass change gas sensors which employ a quartz crystal microbalance (QCM) are popular and widely used in industry. QCM sensors exploit the quantitative relationship between the change in frequency of a quartz crystal resonator and the mass change resulting from the adsorption of analyte gas molecules on the QCM.[250] Crucially, the quartz surface can be coated with an appropriate film to enhance the sensitivity and selectivity of the sensor.[251,252] The advantage of QCM sensors is that they are susceptible to mass changes in the nano-gram range. However, fragility can present challenges.[253] Porous materials such as silicas and MOFs have been used as coatings on the quartz surface to improve the performance of QCM sensors.[234] However, it is worth mentioning that gravimetric detection exhibits drawbacks related to low selectivity.

For example, the isostructural fluorinated MOFs KAUST-7 ([Ni(NbOF$_5$)(pyrazine)$_2$]·2H$_2$O) and KAUST-8 ([Ni(AlF$_5$(OH$_2$))-(pyrazine)$_2$]·2H$_2$O) were employed as coatings on QCM based SO_2 sensors.[214] The difference between these materials is the presence of $(NbOF_5)^{2-}$ *versus* $(AlF_5(OH_2))^{2-}$ within the framework. The authors noted that KAUST-7 exhibits a high affinity for SO_2, SCXRD confirms that SO_2 interacts with two electronegative fluorine atoms of the adjacent $(NbOF_5)^{2-}$ moiety *via* the electropositive sulfur atom, while four C–H···O contacts stabilize the interaction. Meanwhile, in KAUST-8, the SO_2 molecule only interacts with four C–H···O from two neighboring pyrazines. Based on these properties, the materials were studied for SO_2 detection in the presence and absence of humidity to mimic atmospheric conditions. Following the change in frequency of the quartz crystal resonator, SO_2 was successfully detected at concentrations between 0 and 500 ppm in balance with nitrogen. The system exhibited with high stability and reproducibility. Both MOF-coated materials show a nonlinear decrease in sensitivity with the increased SO_2 concentration. The lowest detection limit was estimated to be about 100 ppb with noise drift in the resonance frequency of ±1.5 Hz. However, the experimental lowest detection limit was 5 ppm.

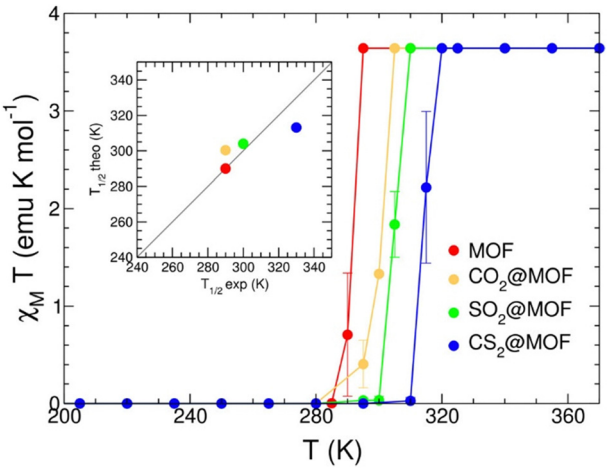

Fig. 19 Temperature dependence of $\chi_M T$ calculated from MC/MD simulations of {Fe(PZ)[Pt(CN)$_4$]} with no adsorbed guest molecules (MOF) as well as upon adsorption of CO_2 (CO_2@MOF), SO_2 (SO_2@MOF), and CS_2 (CS_2@MOF). The theoretical values of the SCO temperature ($T_{1/2}$) are compared in the inset with the experimental values. (Reproduced from ref. 213 Copyright 2018 with permission from American Chemical Society).

4. Overview of SO_2 detection methodology

Considering the discussion above, it is evident that metal–organic frameworks and coordination polymers are well suited for application in gas sensors and detectors. Notably, and unlike many other applications proposed for MOFs, high surface area or elevated gas uptake is not imperative for sensing. Thus, materials deemed unsuitable for "traditional" adsorption applications may find utility in sensing and detection processes where chemical robustness and functionality are prized over uptake capacity. As discussed in this review, the ideal MOF for sensing is stable under relevant working conditions and exhibits a precise and reproducible physical response upon interaction with the analyte at environmental concentrations. Considering these metrics, various devices designed for SO_2 detection were discussed (Fig. 20). These were primarily based on (i) nanofiber membranes, (ii) electrodes, and (iii) test strips.

Below (Fig. 21), the most relevant characterization techniques are evaluated for their potential in gas sensing applications.

(a) Fluorescence measurements: given the broad applicability, high selectivity, and potential for use in super-resolution experiments, fluorescence is one of the most commonly used

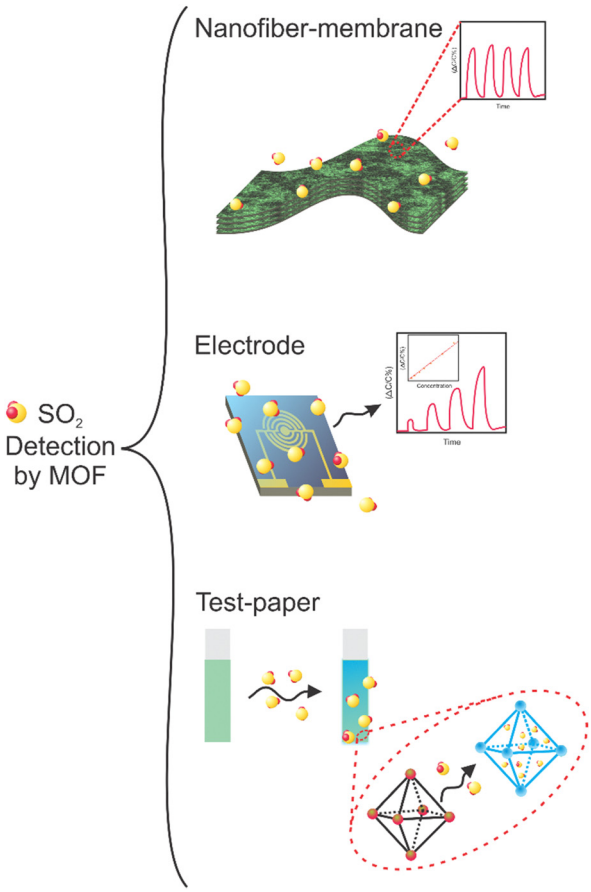

Fig. 20 MOFs applied in different assembled devices for SO_2 detection.

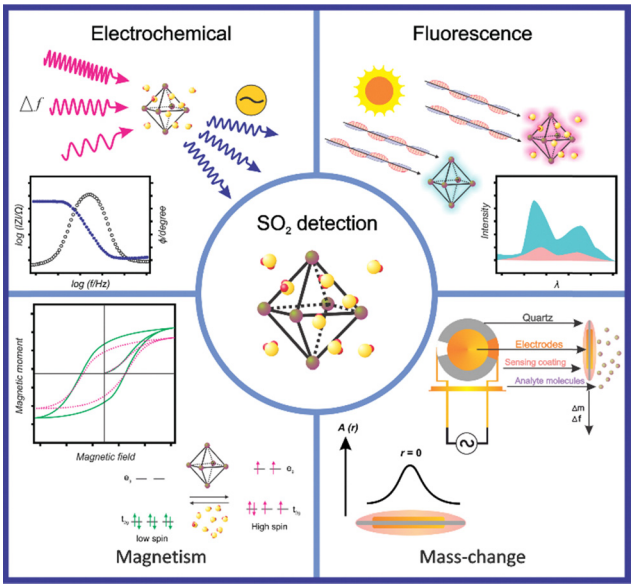

Fig. 21 MOFs applied in different characterization techniques for SO_2 detection.

chemo-sensing techniques.[254] Some fluorescence measurement techniques which are frequently encountered include:

(i) Fluorescence spectroscopy: this technique involves measuring the emission spectrum of a MOF before and after gas adsorption. The change in fluorescence intensity or wavelength can be used to detect and quantify the presence of gas molecules and determine the selectivity of the MOF towards the analyte of interest.[255]

(ii) Time-resolved fluorescence spectroscopy: this technique involves measuring the decay time of the fluorescence emission of a MOF after excitation. The change in decay time upon gas adsorption can be used to detect and quantify the presence of gas molecules and determine the selectivity of the MOF towards the analyte of interest.[196]

(b) Electrochemical measurements: another possible physical response that can be used to sense or detect gaseous molecules is the change in the material's conductivity (or resistivity). The sorption of gas molecules can alter the electrical conductivity of MOFs, which can be measured to detect (and even quantify the concentration of) specific gas molecules. MOFs provide an ideal platform for gas sensing and detection using this technique.[256] However, it must be noted that most MOFs and coordination polymers have very high resistivity and, thus, are not amenable to this kind of measurement. Some of the commonly used conductivity measurements are:

(i) Two and four-point probe measurements: this technique involves applying a voltage to the MOF and measuring the current flowing through it. Thus, the resistivity and conductivity of the MOF can be calculated from the measured values. The measurement can be performed in single crystals, films, or pellets of polycrystalline materials. However, special care must be taken to ensure that the contacts do not interfere with gas sorption and that a reproducible contact is made between the sample and electrodes.[257,258]

(ii) Impedance spectroscopy: this technique involves applying an AC voltage to the MOF and measuring the impedance of the MOF as a function of frequency. The frequency-dependent impedance can provide information about the charge transport properties of the MOF. Similarly, the measurement can be performed in single crystals, thin films, or press pellets. Once again, changes in these properties can be induced by the sorption of the analyte, providing a probe for the detection and quantification of analyte gases.[259,260]

(iii) Field effect transistors (FETs): when a MOF is used as the active material in a FET, changes in the conductivity of the framework upon gas adsorption can be measured using the FET. However, unlike the previous techniques, this measurement is not amenable to polycrystalline samples; instead, MOF single crystals or films are required, which, depending on the material, could pose a synthetic bottleneck.[261,262]

(c) Magnetism measurements: this technique is premised on the fact that the magnetic properties of certain materials will change during sorption of analyte molecules. Changes in magnetic properties can be measured using a variety of sophisticated techniques and related to the concentration of analyte gas.[263,264]

(d) Mass-change: the change of mass that a material, such as a MOF, experiences after the adsorption of a specific gas can be used to evaluate the presence and/or concentration of that gas.

(e) Other techniques: other techniques are used case-by-case to evaluate, study, and apply MOFs as sensors. Some examples are UV-vis absorption, calorimetry, and many others.[265,266]

A comprehensive understanding of these techniques is essential to designing and optimizing MOF-based gas sensors and detectors.

Conclusions

A select class of Metal–organic Frameworks possess high surface area, well-defined pore distribution, and high thermal and chemical stability. In light of these properties, it is not surprising that MOFs have recently garnered significant interest in detection and sensing research. Of particular interest is the detection of SO_2, a hazardous gas to which several chemically stable MOFs have demonstrated promising compatibility. Most SO_2 related MOF research has concentrated on SO_2 adsorption capacity, emphasizing the highest uptake capacity. This is typically reported in conjunction with comprehensive computational and experimental studies that aim to elucidate the specific chemical and physical interactions between SO_2 and the framework with a view to identifying the preferential adsorption sites. This approach has been successfully used for a wide range of materials, yielding valuable insight into the nature of SO_2 adsorption in porous materials. However, in the context of SO_2 detection, both the SO_2 affinity of the framework and the SO_2 adsorption capacity at low pressure must be considered – rather than overall uptake at high pressure. Thus, it is necessary to explore characteristics of MOFs pertinent to SO_2 detection, which typically diverge from those that promote large SO_2 uptake at high pressure. Higher SO_2 uptake at low pressure reflects stronger SO_2 interactions within the framework; this is critical to the operation of SO_2 detectors under environmental conditions since relatively low SO_2 concentrations of $\leq$5000 ppm are typically relevant for sensing. Analysis of the most effective MOFs for SO_2 capture has demonstrated a clear correlation between SO_2 capture at low pressure (0.01 bar) and the pore-limiting diameter.

We have provided an overview of techniques used to perform SO_2 detection in MOFs and evaluated which MOF candidates are likely to perform best. In addition to a high adsorption capacity at low pressure and requisite chemical stability, MOFs require distinct characteristics to selectively detect specific analytes such as SO_2. MOF-based analyte detection is predicated on quantitative (or, in some cases, qualitative) measurement of the response to a particular environmental stimulus (*i.e.*, SO_2 adsorption). As we have outlined, the response typically consists of changes in luminescence, electrochemical properties, or magnetism. Examples of MOF based SO_2 detection using these methodologies have been reported and outlined in detail in the main text. Cruicially, advancement in materials processing combined with excellent chemical stability allow select MOFs to be incorporated into detectors based on nanofiber membranes, electrodes, and test strips.

This review provides a broad overview of the significant role that chemically stable MOFs will play in the expanding field of SO_2 detection. The extraordinary diversity of physiochemical properties displayed by MOFs provides space for chemists to further refine MOF-SO_2 interactions, guided by new characterisation techniques and supported by advanced computational tools. The insights garnered from this process will inform the design of future MOF-based detectors for SO_2 and other volatile compounds.

List of abbreviations

AIP	5-Aminoisophthalate
ATT	3-Amino-1,2,4-triazole-5-thiol
ADC	Acetylenedicarboxylate
BET	Brunauer–Emmett–Teller
BTC	Benzene-1,3,5-tricarboxylate, trimesate
BDC	1,4-Benzenedicarboxylate, terephthalate
BDC-Br	2-Bromoterephthalate
BDC-NH_2	2-Aminoterephthalate
BDC-CH$=$$CH_2$	2-Vinylterephthalate
BDC-NO_2	2-Nitroterephthalate
BDC-4F	2,3,5,6-Tetrafluoro-1,4-benzenedicarboxylate
BPDC	4,4′-Biphenyldicarboxylate
BPTC	Biphenyl-3,3′,5,5′-tetracarboxylate
BTEC	1,2,4,5-Benzenetetracarboxylate
BDP	1,4-Bis(4-pyrazolyl)benzene
CPE	Carbon paste electrode
CDC	9*H*-Carbazole-3,6-dicarboxylate
CD	Carbon dot
CYCU	Chung-Yuan Christian University
CAU	Christian-Albrechts-University
CUK	Cambridge-University-KRICT
CNT	Carbon nanotubes
DFT	Density functional theory
DUT	Dresden University of Technology
DOBPDC	4,4-Dioxidobiphenyl-3,3-dicarboxylate
DABCO	1,4-Diazabicyclo[2,2,2]octane
DHTP	2,5-Dihydroxyterephthalate
DRIFTS	Diffuse reflectance infrared Fourier transform spectroscopy
ETTA	4,4′,4″,4‴-(Ethene-1,1,2,2-tetrayl)tetrabenzoicate
ET-LMOF	Energy transfer LMOFs
GCMC	Grand canonical Monte Carlo
GAL	Gallate
FTIR	Fourier transform infrared
FDCA	2,5-Furandicarboxylate
Fum	Fumarate
FGD	Flue-gas desulfurization
HS	High-spin
HSAB	Pearson's hard-soft acid–base theory
HHTP	2,3,5,6,10,11-Hexahydroxytriphenylene
HATP	2,3,6,7,10,11-Hexaaminotriphenylene
HKUST	Hong Kong University of Science and Technology

LMOFs	Luminescent metal–organic frameworks
LOD	Limit of detection
NDC-$(NO_2)_2$	4,8-Dinitronaphthalene-2,6-dicarboxylate
NDC	1,4-Naphthalenedicarboxylate
NOTT	Nottingham University
NU	Northwestern University
IRMOF	Isoreticular metal–organic framework
MOCs	Metal–organic cages
MOFs	Metal–organic frameworks
MIL	Matériaux de l' Institut Lavoisier
MFM	Manchester framework material
MUF	Massey University Framework
MPBA	*N*,*N*′-2,4,6-Trimethyl-1,3-phenylenebis(oxamate)
OTf	Trifuoromethanesulfonate
THBA	2,3,4-Trihydroxybenzaldehyde
TBAPy	4,4′,4″,4‴-(Pyrene-1,3,6,8-tetrayl)tetrabenzoate
TCPP	*meso*-Tetrakis(4-carboxylphenyl)porphyrin
TDC	2,5-Thiophenedicarboxylate
TBA	4-(4*H*-1,2,4-Triazol-4-yl)benzoate
TRPL	Time-resolved photoluminescence
LS	Low-spin
LOD	Limit of detection
TATB	2,4,6-Tris(4-carboxyphenyl)-1,3,5-triazine
TDC	2,5-Thiophenedicarboxylate
SDC	4,4′-Stilbenedicarboxylate
SCO	Spin-crossover
ppm	Parts per million
ppb	Parts per billion
POCs	Porous organic cages
PAN	Polyacrylonitrile
PAC	*meso*-Tetrakis(4-carboxylphenyl)porphyrin
PA	*m*-Phthalate
PDDB	4,4′-(Pyridine-2,6-diyl)dibenzoate
PHEN	1,10-Phenanthroline
PBTA	4,4′4″,4‴-(4,4′-(1,4-Phenylene)bis (pyridine-6,4,2-triyl))-tetrabenzoate
PCN	Porous coordination network
PPTA	4,4′,4″,4‴-(1,4-Phenylenebis(pyridine-4,2,6-triyl))tetrabenzoate
PXRD	Powder X-ray diffraction
PDCA	2,4-Pyridinedicarboxylate
PLD	Pore limiting diameter
PVDF	Polyvinylidene fluoride
PTBA	4,4′,4″,4‴-(1,4-Phenylenebis(azanetriyl))tetrabenzoate
PZDC	1*H*-Pyrazole-3,5-dicarboxylate
UiO	Universitetet i Oslo
SCXRD	Single-crystal X-ray diffraction
ZIF	Zeolitic imidazolate framework

Data availability

All data is available in the main text.

Conflicts of interest

There are no conflicts to declare.

Acknowledgements

J. L. O. and C. V. F. thanks CONAHCYT for the PhD fellowship (1003953 and 1040318). I. A. I. thanks PAPIIT-UNAM (IN201123), México, for financial support. We thank U. Winnberg (Euro Farmacos EIR) for scientific discussions and G. Ibarra-Winnberg for scientific encouragement. C. J. thanks the DFG for funding within the Priority Program SPP 1928/2 COORNETs (grant Ja466/43-1).

References

1 L. Bai, J. Wang, X. Ma and H. Lu, *Int. J. Environ. Res. Public Health*, 2018, **15**, 780.
2 M. Höök and X. Tang, *Energy Policy*, 2013, **52**, 797–809.
3 B. Zhang and G. Chen, *Process Saf. Environ. Prot.*, 2010, **88**, 253–262.
4 N. Abas, A. Kalair and N. Khan, *Futures*, 2015, **69**, 31–49.
5 F. Perera, *Int. J. Environ. Res. Public Health*, 2017, **15**, 16.
6 M. E. Quesada-Valverde and A. Quesada-Román, *Geosciences*, 2023, **13**, 39.
7 A. N. Torres, A. L. M. Del Pozzo, G. Groppelli and M. Del Carmen Jaimes Viera, *J. Volcanol. Geotherm. Res.*, 2023, **433**, 107733.
8 S. Valade, D. Coppola, R. Campion, A. Ley, T. Boulesteix, N. Taquet, D. Legrand, M. Laiolo, T. R. Walter and S. De La Cruz-Reyna, *Nat. Commun.*, 2023, **14**, 3254.
9 B. Divol, M. Du Toit and E. Duckitt, *Appl. Microbiol. Biotechnol.*, 2012, **95**, 601–613.
10 E. Calabrese, C. Sacco, G. Moore and S. DiNardi, *Med. Hypotheses*, 1981, **7**, 133–145.
11 P. Amoatey, H. Omidvarborna, M. S. Baawain and A. Al-Mamun, *Process Saf. Environ. Prot.*, 2019, **123**, 215–228.
12 R. J. Melia, C. D. Florey and A. V. Swan, *J. Epidemiol. Community Health*, 1981, **35**, 161–167.
13 W. Van Roy, B. Van Roozendael, L. Vigin, A. Van Nieuwenhove, K. Scheldeman, J.-B. Merveille, A. Weigelt, J. Mellqvist, J. Van Vliet, D. Van Dinther, J. Beecken, F. Tack, N. Theys and F. Maes, *Commun. Earth Environ.*, 2023, **4**, 391.
14 V. Jonas, G. Frenking and M. T. Reetz, *J. Am. Chem. Soc.*, 1994, **116**, 8741–8753.
15 T. P. Cunningham, D. L. Cooper, J. Gerratt, P. B. Karadakov and M. Raimondi, *J. Chem. Soc., Faraday Trans.*, 1997, **93**, 2247–2254.
16 D. Patel, D. Margolese and T. R. Dykea, *J. Chem. Phys.*, 1979, **70**, 2740–2747.
17 I. Jana, S. Naskar and D. Nandi, *J. Phys.:Conf. Ser.*, 2020, **1412**, 052005.
18 Y. Qu, J. An, Y. He and J. Zheng, *J. Environ. Sci.*, 2016, **44**, 13–25.
19 M. M. M. F. Jion, J. N. Jannat, M. Y. Mia, M. A. Ali, M. S. Islam, S. M. Ibrahim, S. C. Pal, A. Islam, A. Sarker,

G. Malafaia, M. Bilal and A. R. M. T. Islam, *Sci. Total Environ*, 2023, **876**, 162851.
20 N. D. Abdul Halim, M. T. Latif, F. Ahamad, D. Dominick, J. X. Chung, L. Juneng and M. F. Khan, *Heliyon*, 2018, **4**, e01054.
21 M. Ali and M. Athar, *Environ. Monit. Assess.*, 2010, **171**, 353–363.
22 Z.-Y. Meng, X.-B. Xu, T. Wang, X.-Y. Zhang, X.-L. Yu, S.-F. Wang, W.-L. Lin, Y.-Z. Chen, Y.-A. Jiang and X.-Q. An, *Atmos. Environ.*, 2010, **44**, 2625–2631.
23 C. Mallik and S. Lal, *Environ. Monit. Assess.*, 2014, **186**, 1295–1310.
24 S. S. Mousavi, G. Goudarzi, S. Sabzalipour, M. M. Rouzbahani and E. Mobarak Hassan, *Environ. Sci. Pollut. Res.*, 2021, **28**, 56996–57008.
25 B. J. Freedman, *Br. J. Dis. Chest*, 1980, **74**, 128–134.
26 S. Giacosa, S. Río Segade, E. Cagnasso, A. Caudana, L. Rolle and V. Gerbi, *Red Wine Technology*, Elsevier, 2019, pp. 309–321.
27 P. Mars, *J. Catal.*, 1968, **10**, 1–12.
28 F. García-Labiano, L. F. De Diego, A. Cabello, P. Gayán, A. Abad, J. Adánez and G. Sprachmann, *Appl. Energy*, 2016, **178**, 736–745.
29 A. S. Milev, G. S. K. Kannangara and M. A. Wilson, in *Kirk-Othmer Encyclopedia of Chemical Technology*, ed. Kirk-Othmer, Wiley, 1st edn, 2005.
30 R. Saidur, M. Sattar, H. H. Masjuki and M. Y. Jamaluddin, *Energy Environ.*, 2009, **20**, 533–551.
31 S. Piché, F. Larachi and B. P. A. Grandjean, *Ind. Eng. Chem. Res.*, 2001, **40**, 476–487.
32 F. W. Adams, *Ind. Eng. Chem.*, 1933, **25**, 424–428.
33 B. Hanley and C. Chen, *AIChE J.*, 2012, **58**, 132–152.
34 M. Reda and G. R. Carmichael, *Atmos. Environ.*, 1982, **16**, 151–159.
35 R. K. Srivastava, W. Jozewicz and C. Singer, *Environ. Prog.*, 2001, **20**, 219–228.
36 D. B. Gingerich, E. Grol and M. S. Mauter, *Environ. Sci.: Water Res. Technol.*, 2018, **4**, 909–925.
37 P. Luis, A. Garea and A. Irabien, *J. Membr. Sci.*, 2009, **330**, 80–89.
38 Y. Sun, J. Xie, W. Huang, G. Li, S. Li, P. Cui, H. Xu, Z. Qu and N. Yan, *Fuel*, 2021, **288**, 119714.
39 Q. Xin, C. Zhang, Y. Zhang, Q. Liang, L. Zhang, S. Wang, H. Ye, X. Ding and Y. Zhang, *Sep. Purif. Technol.*, 2021, **259**, 118222.
40 P. Luis, A. Garea and A. Irabien, *J. Chem. Technol. Biotechnol.*, 2008, **83**, 1570–1577.
41 H.-K. Lee, B. R. Deshwal and K.-S. Yoo, *Korean J. Chem. Eng.*, 2005, **22**, 208–213.
42 Y. A. Husnil, R. Andika and M. Lee, *J. Process Control*, 2019, **74**, 147–159.
43 W. Liu, R. D. Vidic and T. D. Brown, *Environ. Sci. Technol.*, 2000, **34**, 154–159.
44 H. Yi, H. Deng, X. Tang, Q. Yu, X. Zhou and H. Liu, *J. Hazard. Mater.*, 2012, **203–204**, 111–117.
45 H. Fu, X. Wang, H. Wu, Y. Yin and J. Chen, *J. Phys. Chem. C*, 2007, **111**, 6077–6085.
46 Y. Li, L. Li and J. Yu, *Chem*, 2017, **3**, 928–949.
47 S. Beyaz Kayiran and F. Lamari Darkrim, *Surf. Interface Anal.*, 2002, **34**, 100–104.
48 E. Pérez-Botella, S. Valencia and F. Rey, *Chem. Rev.*, 2022, **122**, 17647–17695.
49 Y. Tao, H. Kanoh, L. Abrams and K. Kaneko, *Chem. Rev.*, 2006, **106**, 896–910.
50 N. K. Gupta, E. J. Kim, S. Baek, J. Bae and K. S. Kim, *Sci. Rep.*, 2022, **12**, 15387.
51 C. Petit, *Curr. Opin. Chem. Eng.*, 2018, **20**, 132–142.
52 J. L. Obeso, D. R. Amaro, C. V. Flores, A. Gutiérrez-Alejandre, R. A. Peralta, C. Leyva and I. A. Ibarra, *Coord. Chem. Rev.*, 2023, **485**, 215135.
53 A. Carné-Sánchez, J. Martínez-Esaín, T. Rookard, C. J. Flood, J. Faraudo, K. C. Stylianou and D. Maspoch, *ACS Appl. Mater. Interfaces*, 2023, **15**, 6747–6754.
54 E. Martínez-Ahumada, D. He, V. Berryman, A. López-Olvera, M. Hernandez, V. Jancik, V. Martis, M. A. Vera, E. Lima, D. J. Parker, A. I. Cooper, I. A. Ibarra and M. Liu, *Angew. Chem., Int. Ed.*, 2021, **60**, 17556–17563.
55 J. L. Obeso, A. López-Olvera, C. V. Flores, E. Martínez-Ahumada, R. Paz, H. Viltres, A. Islas-Jácome, E. González-Zamora, J. Balmaseda, S. López-Morales, M. A. Vera, E. Lima, I. A. Ibarra and C. Leyva, *J. Mol. Liq.*, 2022, **368**, 120758.
56 S. R. Batten, N. R. Champness, X.-M. Chen, J. Garcia-Martinez, S. Kitagawa, L. Öhrström, M. O'Keeffe, M. Paik Suh and J. Reedijk, *Pure Appl. Chem.*, 2013, **85**, 1715–1724.
57 S. R. Batten, N. R. Champness, X.-M. Chen, J. Garcia-Martinez, S. Kitagawa, L. Öhrström, M. O'Keeffe, M. P. Suh and J. Reedijk, *CrystEngComm*, 2012, **14**, 3001.
58 S. L. James, *Chem. Soc. Rev.*, 2003, **32**, 276.
59 H.-C. Joe Zhou and S. Kitagawa, *Chem. Soc. Rev.*, 2014, **43**, 5415–5418.
60 N. K. Gupta, A. López-Olvera, E. González-Zamora, E. Martínez-Ahumada and I. A. Ibarra, *ChemPlusChem*, 2022, **87**, e202200006.
61 J. L. Obeso, H. Viltres, C. V. Flores, A. López-Olvera, A. R. Rajabzadeh, S. Srinivasan, I. A. Ibarra and C. Leyva, *J. Environ. Chem. Eng.*, 2023, **11**, 109872.
62 J. L. Obeso, V. B. López-Cervantes, C. V. Flores, H. Viltres, C. Serrano-Fuentes, L. Herrera-Zuñiga, N. S. Portillo-Vélez, R. A. Peralta, D. Solis-Ibarra, I. A. Ibarra and C. Leyva, *ACS Sustainable Resour. Manage.*, 2024, **1**, 661–669.
63 C. V. Flores, J. L. Obeso, H. Viltres, R. A. Peralta, I. A. Ibarra and C. Leyva, *Environ. Sci.: Water Res. Technol.*, 2024, **10**, 2142–2147.
64 J. L. Obeso, J. G. Flores, C. V. Flores, V. B. López-Cervantes, V. Martínez-Jiménez, J. A. De Los Reyes, E. Lima, D. Solis-Ibarra, I. A. Ibarra, C. Leyva and R. A. Peralta, *Dalton Trans.*, 2023, **52**, 12490–12495.
65 J. G. Flores, J. L. Obeso, V. Martínez-Jiménez, N. Martín-Guaregua, A. Islas-Jácome, E. González-Zamora, H. Serrano-Espejel, B. Mondragón-Rodríguez, C. Leyva, D. A. Solís-Casados, I. A. Ibarra, R. A. Peralta, J. Aguilar-Pliego and J. Antonio De Los Reyes, *RSC Adv.*, 2023, **13**, 27174–27179.

66 V. Pascanu, G. González Miera, A. K. Inge and B. Martín-Matute, *J. Am. Chem. Soc.*, 2019, **141**, 7223–7234.
67 S. Rojas, I. Colinet, D. Cunha, T. Hidalgo, F. Salles, C. Serre, N. Guillou and P. Horcajada, *ACS Omega*, 2018, **3**, 2994–3003.
68 E. Medel, J. L. Obeso, C. Serrano-Fuentes, J. Garza, I. A. Ibarra, C. Leyva, A. K. Inge, A. Martínez and R. Vargas, *Chem. Commun.*, 2023, **59**, 8684–8687.
69 S. Bügel, Q.-D. Hoang, A. Spieß, Y. Sun, S. Xing and C. Janiak, *Membranes*, 2021, **11**, 795.
70 H. B. Tanh Jeazet, C. Staudt and C. Janiak, *Dalton Trans.*, 2012, **41**, 14003.
71 B. Gil-Hernández, S. Millan, I. Gruber, M. Quirós, D. Marrero-López, C. Janiak and J. Sanchiz, *Inorg. Chem.*, 2022, **61**, 11651–11666.
72 B. Gil-Hernández, P. Gili, J. K. Vieth, C. Janiak and J. Sanchiz, *Inorg. Chem.*, 2010, **49**, 7478–7490.
73 X. Han, S. Yang and M. Schröder, *Nat. Rev. Chem.*, 2019, **3**, 108–118.
74 S. Han, Y. Huang, T. Watanabe, S. Nair, K. S. Walton, D. S. Sholl and J. Carson Meredith, *Microporous Mesoporous Mater.*, 2013, **173**, 86–91.
75 G. Mouchaham, S. Wang and C. Serre, in *Metal-Organic Frameworks*, ed. H. García and S. Navalón, Wiley, 1st edn, 2018, pp. 1–28.
76 K. O. Kirlikovali, S. L. Hanna, F. A. Son and O. K. Farha, *ACS Nanosci. Au*, 2023, **3**, 37–45.
77 R. G. Pearson, *J. Am. Chem. Soc.*, 1963, **85**, 3533–3539.
78 Y. Jin, H. Liu, M. Feng, Q. Ma and B. Wang, *Adv. Funct. Mater.*, 2023, 2304773.
79 I. Senkovska and S. Kaskel, *Chem. Commun.*, 2014, **50**, 7089.
80 J. Valdes-García, L. D. Rosales-Vázquez, I. J. Bazany-Rodríguez and A. Dorazco-González, *Chem. – Asian J.*, 2020, **15**, 2925–2938.
81 C. Bargossi, M. C. Fiorini, M. Montalti, L. Prodi and N. Zaccheroni, *Coord. Chem. Rev.*, 2000, **208**, 17–32.
82 H.-Y. Li, S.-N. Zhao, S.-Q. Zang and J. Li, *Chem. Soc. Rev.*, 2020, **49**, 6364–6401.
83 Y. Jian, W. Hu, Z. Zhao, P. Cheng, H. Haick, M. Yao and W. Wu, *Nano-Micro Lett.*, 2020, **12**, 71.
84 G. Yang, X. Jiang, H. Xu and B. Zhao, *Small*, 2021, **17**, 2005327.
85 Y. Wang, Y. Zhu, A. Binyam, M. Liu, Y. Wu and F. Li, *Biosens. Bioelectron.*, 2016, **86**, 432–438.
86 Y. T. Azar, M. S. Lakmehsari, S. M. Kazem Manzoorolajdad, V. Sokhanvaran, Z. Ahadi, A. Shahsavani and P. K. Hopke, *Mater. Chem. Phys.*, 2020, **239**, 122105.
87 W.-T. Koo, J.-S. Jang and I.-D. Kim, *Chem*, 2019, **5**, 1938–1963.
88 Y. Li, S. Zhang and D. Song, *Angew. Chem., Int. Ed.*, 2013, **52**, 710–713.
89 R. Lin, S. Liu, J. Ye, X. Li and J. Zhang, *Adv. Sci.*, 2016, **3**, 1500434.
90 N. B. Shustova, A. F. Cozzolino, S. Reineke, M. Baldo and M. Dincă, *J. Am. Chem. Soc.*, 2013, **135**, 13326–13329.
91 X. Li, B. Liu, K. Ye, L. Ni, X. Xu, F. Qiu, J. Pan and X. Niu, *Sens. Actuators, B*, 2019, **297**, 126822.
92 Z.-P. Ni, J.-L. Liu, Md. N. Hoque, W. Liu, J.-Y. Li, Y.-C. Chen and M.-L. Tong, *Coord. Chem. Rev.*, 2017, **335**, 28–43.
93 A. Tissot, X. Kesse, S. Giannopoulou, I. Stenger, L. Binet, E. Rivière and C. Serre, *Chem. Commun.*, 2019, **55**, 194–197.
94 P. D. Southon, L. Liu, E. A. Fellows, D. J. Price, G. J. Halder, K. W. Chapman, B. Moubaraki, K. S. Murray, J.-F. Létard and C. J. Kepert, *J. Am. Chem. Soc.*, 2009, **131**, 10998–11009.
95 N. Kau, G. Jindal, R. Kaur and S. Rana, *Results Chem.*, 2022, **4**, 100678.
96 P. Samanta, S. Let, W. Mandal, S. Dutta and S. K. Ghosh, *Inorg. Chem. Front.*, 2020, **7**, 1801–1821.
97 H. Zhou, X. Hui, D. Li, D. Hu, X. Chen, X. He, L. Gao, H. Huang, C. Lee and X. Mu, *Adv. Sci.*, 2020, **7**, 2001173.
98 G. Ji, T. Zheng, X. Gao and Z. Liu, *Sens. Actuators, B*, 2019, **284**, 91–95.
99 W.-J. Ju, L.-M. Fu, R.-J. Yang and C.-L. Lee, *Lab Chip*, 2012, **12**, 622–626.
100 T. R. Khan and J. C. Meranger, *Environ. Int.*, 1983, **9**, 195–206.
101 P. Popp and G. Oppermann, *J. Chromatogr. A*, 1981, **207**, 131–137.
102 W. L. Crider, *Anal. Chem.*, 1965, **37**, 1770–1773.
103 M. S. Yogendra Kumar, M. D. Gowtham, Mahadevaiah and G. Nagendrappa, *Anal. Sci.*, 2006, **22**, 757–761.
104 Y. Wen, P. Zhang, V. K. Sharma, X. Ma and H.-C. Zhou, *Cell Rep.*, 2021, **2**, 100348.
105 O. D. Agboola and N. U. Benson, *Front. Environ. Sci.*, 2021, **9**, 678574.
106 E. Martínez-Ahumada, M. L. Díaz-Ramírez, M. D. J. Velásquez-Hernández, V. Jancik and I. A. Ibarra, *Chem. Sci.*, 2021, **12**, 6772–6799.
107 A. J. Rieth, A. M. Wright and M. Dincă, *Nat. Rev. Mater.*, 2019, **4**, 708–725.
108 Q. Zhang, H. Yang, T. Zhou, X. Chen, W. Li and H. Pang, *Adv. Sci.*, 2022, **9**, 2204141.
109 X.-D. Song, S. Wang, C. Hao and J.-S. Qiu, *Inorg. Chem. Commun.*, 2014, **46**, 277–281.
110 E. Martínez-Ahumada, A. López-Olvera, V. Jancik, J. E. Sánchez-Bautista, E. González-Zamora, V. Martis, D. R. Williams and I. A. Ibarra, *Organometallics*, 2020, **39**, 883–915.
111 G. J. Kubas, *Inorg. Chem.*, 1979, **18**, 182–188.
112 D. Kim, M. Kang, H. Ha, C. S. Hong and M. Kim, *Coord. Chem. Rev.*, 2021, **438**, 213892.
113 Y. Lin, C. Kong and L. Chen, *RSC Adv.*, 2016, **6**, 32598–32614.
114 S. Yang, J. Sun, A. J. Ramirez-Cuesta, S. K. Callear, W. I. F. David, D. P. Anderson, R. Newby, A. J. Blake, J. E. Parker, C. C. Tang and M. Schröder, *Nat. Chem.*, 2012, **4**, 887–894.
115 J. H. Carter, C. G. Morris, H. G. W. Godfrey, S. J. Day, J. Potter, S. P. Thompson, C. C. Tang, S. Yang and M. Schröder, *ACS Appl. Mater. Interfaces*, 2020, **12**, 42949–42954.
116 J. A. Zárate, E. Sánchez-González, D. R. Williams, E. González-Zamora, V. Martis, A. Martínez, J. Balmaseda, G. Maurin and I. A. Ibarra, *J. Mater. Chem. A*, 2019, **7**, 15580–15584.

117 M. Savage, Y. Cheng, T. L. Easun, J. E. Eyley, S. P. Argent, M. R. Warren, W. Lewis, C. Murray, C. C. Tang, M. D. Frogley, G. Cinque, J. Sun, S. Rudić, R. T. Murden, M. J. Benham, A. N. Fitch, A. J. Blake, A. J. Ramirez-Cuesta, S. Yang and M. Schröder, *Adv. Mater.*, 2016, **28**, 8705–8711.
118 A. López-Olvera, J. A. Zárate, E. Martínez-Ahumada, D. Fan, M. L. Díaz-Ramírez, P. A. Sáenz-Cavazos, V. Martis, D. R. Williams, E. Sánchez-González, G. Maurin and I. A. Ibarra, *ACS Appl. Mater. Interfaces*, 2021, **13**, 39363–39370.
119 A. López-Olvera, S. Pioquinto-García, J. Antonio Zárate, G. Diaz, E. Martínez-Ahumada, J. L. Obeso, V. Martis, D. R. Williams, H. A. Lara-García, C. Leyva, C. V. Soares, G. Maurin, I. A. Ibarra and N. E. Dávila-Guzmán, *Fuel*, 2022, **322**, 124213.
120 S. G. Dunning, N. K. Gupta, J. E. Reynolds, M. Sagastuy-Breña, J. G. Flores, E. Martínez-Ahumada, E. Sánchez-González, V. M. Lynch, A. Gutiérrez-Alejandre, J. Aguilar-Pliego, K.-S. Kim, I. A. Ibarra and S. M. Humphrey, *Inorg. Chem.*, 2022, **61**, 15037–15044.
121 P. Brandt, A. Nuhnen, M. Lange, J. Möllmer, O. Weingart and C. Janiak, *ACS Appl. Mater. Interfaces*, 2019, **11**, 17350–17358.
122 C. Jansen, N. Tannert, D. Lenzen, M. Bengsch, S. Millan, A. Goldman, D. N. Jordan, L. Sondermann, N. Stock and C. Janiak, *Z. Anorg. Allg. Chem.*, 2022, **648**, e202200170.
123 Ü. Kökçam-Demir, A. Goldman, L. Esrafili, M. Gharib, A. Morsali, O. Weingart and C. Janiak, *Chem. Soc. Rev.*, 2020, **49**, 2751–2798.
124 L. Tao, C.-Y. Lin, S. Dou, S. Feng, D. Chen, D. Liu, J. Huo, Z. Xia and S. Wang, *Nano Energy*, 2017, **41**, 417–425.
125 A. Yadav, S. Kumari, P. Yadav, A. Hazra, A. Chakraborty and P. Kanoo, *Dalton Trans.*, 2022, **51**, 15496–15506.
126 J. H. Choe, H. Kim and C. S. Hong, *Mater. Chem. Front.*, 2021, **5**, 5172–5185.
127 K. Tan, S. Zuluaga, H. Wang, P. Canepa, K. Soliman, J. Cure, J. Li, T. Thonhauser and Y. J. Chabal, *Chem. Mater.*, 2017, **29**, 4227–4235.
128 G. L. Smith, J. E. Eyley, X. Han, X. Zhang, J. Li, N. M. Jacques, H. G. W. Godfrey, S. P. Argent, L. J. McCormick McPherson, S. J. Teat, Y. Cheng, M. D. Frogley, G. Cinque, S. J. Day, C. C. Tang, T. L. Easun, S. Rudić, A. J. Ramirez-Cuesta, S. Yang and M. Schröder, *Nat. Mater.*, 2019, **18**, 1358–1365.
129 W. Li, J. Li, T. D. Duong, S. A. Sapchenko, X. Han, J. D. Humby, G. F. S. Whitehead, I. J. Victórica-Yrezábal, I. Da Silva, P. Manuel, M. D. Frogley, G. Cinque, M. Schröder and S. Yang, *J. Am. Chem. Soc.*, 2022, **144**, 13196–13204.
130 E. Martínez-Ahumada, M. L. Díaz-Ramírez, H. A. Lara-García, D. R. Williams, V. Martis, V. Jancik, E. Lima and I. A. Ibarra, *J. Mater. Chem. A*, 2020, **8**, 11515–11520.
131 O. V. Gutov, M. G. Hevia, E. C. Escudero-Adán and A. Shafir, *Inorg. Chem.*, 2015, **54**, 8396–8400.
132 M. Szufla, J. A. R. Navarro, K. Góra-Marek and D. Matoga, *ACS Appl. Mater. Interfaces*, 2023, **15**, 28184–28192.
133 W. Xiang, Y. Zhang, Y. Chen, C. Liu and X. Tu, *J. Mater. Chem. A*, 2020, **8**, 21526–21546.
134 L. M. Rodríguez-Albelo, E. López-Maya, S. Hamad, A. R. Ruiz-Salvador, S. Calero and J. A. R. Navarro, *Nat. Commun.*, 2017, **8**, 14457.
135 S. Li, W. Han, Q. An, K. Yong and M. Yin, *Adv. Funct. Mater.*, 2023, **33**, 2303447.
136 T. Matemb Ma Ntep, H. Breitzke, L. Schmolke, C. Schlüsener, B. Moll, S. Millan, N. Tannert, I. El Aita, G. Buntkowsky and C. Janiak, *Chem. Mater.*, 2019, **31**, 8629–8638.
137 D. Britt, D. Tranchemontagne and O. M. Yaghi, *Proc. Natl. Acad. Sci. U. S. A.*, 2008, **105**, 11623–11627.
138 S. Glomb, D. Woschko, G. Makhloufi and C. Janiak, *ACS Appl. Mater. Interfaces*, 2017, **9**, 37419–37434.
139 J. H. Carter, X. Han, F. Y. Moreau, I. Da Silva, A. Nevin, H. G. W. Godfrey, C. C. Tang, S. Yang and M. Schröder, *J. Am. Chem. Soc.*, 2018, **140**, 15564–15567.
140 P. Brandt, A. Nuhnen, S. Öztürk, G. Kurt, J. Liang and C. Janiak, *Adv. Sustainable Syst.*, 2021, **5**, 2000285.
141 M. Mon, E. Tiburcio, J. Ferrando-Soria, R. Gil San Millán, J. A. R. Navarro, D. Armentano and E. Pardo, *Chem. Commun.*, 2018, **54**, 9063–9066.
142 F. Chen, D. Lai, L. Guo, J. Wang, P. Zhang, K. Wu, Z. Zhang, Q. Yang, Y. Yang, B. Chen, Q. Ren and Z. Bao, *J. Am. Chem. Soc.*, 2021, **143**, 9040–9047.
143 S. Xing, J. Liang, P. Brandt, F. Schäfer, A. Nuhnen, T. Heinen, I. Boldog, J. Möllmer, M. Lange, O. Weingart and C. Janiak, *Angew. Chem., Int. Ed.*, 2021, **60**, 17998–18005.
144 Y. L. Fan, H. P. Zhang, M. J. Yin, R. Krishna, X. F. Feng, L. Wang, M. B. Luo and F. Luo, *Inorg. Chem.*, 2021, **60**, 4–8.
145 Y.-B. Ren, H.-Y. Xu, S.-Q. Gang, Y.-J. Gao, X. Jing and J.-L. Du, *Chem. Eng. J.*, 2022, **431**, 134057.
146 Y. Zhang, P. Zhang, W. Yu, J. Zhang, J. Huang, J. Wang, M. Xu, Q. Deng, Z. Zeng and S. Deng, *ACS Appl. Mater. Interfaces*, 2019, **11**, 10680–10688.
147 K. Vellingiri, A. Deep and K.-H. Kim, *ACS Appl. Mater. Interfaces*, 2016, **8**, 29835–29857.
148 J.-Y. Lee, T. C. Keener and Y. J. Yang, *J. Air Waste Manage. Assoc.*, 2009, **59**, 725–732.
149 Y. Igarashi, Y. Sawa, K. Yoshioka, H. Matsueda, K. Fujii and Y. Dokiya, *J. Geophys. Res.*, 2004, **109**, 2003JD004428.
150 S. D. Worrall, M. A. Bissett, P. I. Hill, A. P. Rooney, S. J. Haigh, M. P. Attfield and R. A. W. Dryfe, *Electrochim. Acta*, 2016, **222**, 361–369.
151 P. Brandt, S.-H. Xing, J. Liang, G. Kurt, A. Nuhnen, O. Weingart and C. Janiak, *ACS Appl. Mater. Interfaces*, 2021, **13**, 29137–29149.
152 P. Liu, K. Cai, K. Wang, T. Zhao and D.-J. Tao, *Green Energy Environ.*, 2023, S2468025723001309.
153 S. Gorla, M. L. Díaz-Ramírez, N. S. Abeynayake, D. M. Kaphan, D. R. Williams, V. Martis, H. A. Lara-García, B. Donnadieu, N. Lopez, I. A. Ibarra and V. Montiel-Palma, *ACS Appl. Mater. Interfaces*, 2020, **12**, 41758–41764.

154 J. García Ponce, M. L. Díaz-Ramírez, S. Gorla, C. Navarathna, G. Sanchez-Lecuona, B. Donnadieu, I. A. Ibarra and V. Montiel-Palma, *CrystEngComm*, 2021, **23**, 7479–7484.
155 X.-H. Xiong, Z.-W. Wei, W. Wang, L.-L. Meng and C.-Y. Su, *J. Am. Chem. Soc.*, 2023, **145**, 14354–14364.
156 J. Liang, S. Xing, P. Brandt, A. Nuhnen, C. Schlüsener, Y. Sun and C. Janiak, *J. Mater. Chem. A*, 2020, **8**, 19799–19804.
157 Y. Sun, J. Liang, P. Brandt, A. Spieß, S. Öztürk and C. Janiak, *Nanoscale*, 2021, **13**, 15952–15962.
158 N. Tannert, Y. Sun, E. Hastürk, S. Nießing and C. Janiak, *Z. Anorg. Allg. Chem.*, 2021, **647**, 1124–1130.
159 M. D. J. Velásquez-Hernández, V. B. López-Cervantes, E. Martínez-Ahumada, M. Tu, U. Hernández-Balderas, D. Martínez-Otero, D. R. Williams, V. Martis, E. Sánchez-González, J.-S. Chang, J. S. Lee, J. Balmaseda, R. Ameloot, I. A. Ibarra and V. Jancik, *Chem. Mater.*, 2022, **34**, 669–677.
160 L. J. Barrios-Vargas, J. G. Ruiz-Montoya, B. Landeros-Rivera, J. R. Álvarez, D. Alvarado-Alvarado, R. Vargas, A. Martínez, E. González-Zamora, L. M. Cáceres, J. C. Morales and I. A. Ibarra, *Dalton Trans.*, 2020, **49**, 2786–2793.
161 J. A. Zárate, E. Domínguez-Ojeda, E. Sánchez-González, E. Martínez-Ahumada, V. B. López-Cervantes, D. R. Williams, V. Martis, I. A. Ibarra and J. Alejandre, *Dalton Trans.*, 2020, **49**, 9203–9207.
162 A. López-Olvera, H. Montes-Andrés, E. Martínez-Ahumada, V. B. López-Cervantes, R. D. Martínez-Serrano, E. González-Zamora, A. Martínez, P. Leo, C. Martos, I. A. Ibarra and G. Orcajo, *Eur. J. Inorg. Chem.*, 2021, 4458–4462.
163 E. S. Grape, J. G. Flores, T. Hidalgo, E. Martínez-Ahumada, A. Gutiérrez-Alejandre, A. Hautier, D. R. Williams, M. O'Keeffe, L. Öhrström, T. Willhammar, P. Horcajada, I. A. Ibarra and A. K. Inge, *J. Am. Chem. Soc.*, 2020, **142**, 16795–16804.
164 R. Domínguez-González, I. Rojas-León, E. Martínez-Ahumada, D. Martínez-Otero, H. A. Lara-García, J. Balmaseda-Era, I. A. Ibarra, E. G. Percástegui and V. Jancik, *J. Mater. Chem. A*, 2019, **7**, 26812–26817.
165 J. L. Obeso, K. Gopalsamy, M. Wahiduzzaman, E. Martínez-Ahumada, D. Fan, H. A. Lara-García, F. J. Carmona, G. Maurin, I. A. Ibarra and J. A. R. Navarro, *J. Mater. Chem. A*, 2024, **12**, 10157–10165.
166 H. Zhao, X. Gu, T. Yan, G. Han and D. Liu, *AIChE J.*, 2023, **69**, e17942.
167 S.-Q. Gang, Z.-Y. Liu, Y.-N. Bian, R. Wang and J.-L. Du, *Sep. Purif. Technol.*, 2024, **335**, 126153.
168 L. J. Guo, X. F. Feng, Z. Gao, R. Krishna and F. Luo, *Inorg. Chem.*, 2021, **60**, 1310–1314.
169 A. López-Olvera, J. A. Zárate, J. L. Obeso, E. Sánchez-González, J. A. De Los Reyes, R. A. Peralta, E. González-Zamora and I. A. Ibarra, *Inorg. Chem.*, 2023, **62**, 20901–20905.
170 J. Yao, Z. Zhao, L. Yu, J. Huang, S. Shen, S. Zhao, Y. Wu, X. Tian, J. Wang and Q. Xia, *J. Mater. Chem. A*, 2023, **11**, 14728–14737.
171 J. Li, G. L. Smith, Y. Chen, Y. Ma, M. Kippax-Jones, M. Fan, W. Lu, M. D. Frogley, G. Cinque, S. J. Day, S. P. Thompson, Y. Cheng, L. L. Daemen, A. J. Ramirez-Cuesta, M. Schröder and S. Yang, *Angew. Chem., Int. Ed.*, 2022, **61**, e202207259.
172 L. Briggs, R. Newby, X. Han, C. G. Morris, M. Savage, C. P. Krap, T. L. Easun, M. D. Frogley, G. Cinque, C. A. Murray, C. C. Tang, J. Sun, S. Yang and M. Schröder, *J. Mater. Chem. A*, 2021, **9**, 7190–7197.
173 L. Li, I. Da Silva, D. I. Kolokolov, X. Han, J. Li, G. Smith, Y. Cheng, L. L. Daemen, C. G. Morris, H. G. W. Godfrey, N. M. Jacques, X. Zhang, P. Manuel, M. D. Frogley, C. A. Murray, A. J. Ramirez-Cuesta, G. Cinque, C. C. Tang, A. G. Stepanov, S. Yang and M. Schroder, *Chem. Sci.*, 2019, **10**, 1472–1482.
174 X. Cui, Q. Yang, L. Yang, R. Krishna, Z. Zhang, Z. Bao, H. Wu, Q. Ren, W. Zhou, B. Chen and H. Xing, *Adv. Mater.*, 2017, **29**, 1606929.
175 W. Li, C. Cheng, G. Gao, H. Xu, W. Huang, Z. Qu and N. Yan, *Mater. Horiz.*, 2024, **11**, 1889–1898.
176 N. Aboosedgh and S. Fatemi, *J. Environ. Chem. Eng.*, 2024, **12**, 112042.
177 X. Kan, G. Zhang, J. Ma, F. Liu, Y. Tang, F. Liu, X. Yi, Y. Liu, A. Zheng, L. Jiang, F. Xiao and S. Dai, *Adv. Funct. Mater.*, 2024, **34**, 2312044.
178 W. Xu, L. Li, M. Guo, F. Zhang, P. Dai, X. Gu, D. Liu, T. Liu, K. Zhang, T. Xing, M. Wang, Z. Li and M. Wu, *Angew. Chem., Int. Ed.*, 2023, **62**, e202312029.
179 Y. Zhang, Z. Chen, X. Liu, Z. Dong, P. Zhang, J. Wang, Q. Deng, Z. Zeng, S. Zhang and S. Deng, *Ind. Eng. Chem. Res.*, 2020, **59**, 874–882.
180 W. Gong, Y. Xie, A. Yamano, S. Ito, X. Tang, E. W. Reinheimer, C. D. Malliakas, J. Dong, Y. Cui and O. K. Farha, *J. Am. Chem. Soc.*, 2023, **145**, 26890–26899.
181 Z. Zhang, B. Yang and H. Ma, *Sep. Purif. Technol.*, 2021, **259**, 118164.
182 Y. Ma, A. Li and C. Wang, *Chem. Eng. J.*, 2023, **455**, 140687.
183 K. Tan, P. Canepa, Q. Gong, J. Liu, D. H. Johnson, A. Dyevoich, P. K. Thallapally, T. Thonhauser, J. Li and Y. J. Chabal, *Chem. Mater.*, 2013, **25**, 4653–4662.
184 X.-D. Zhang, N. Wang, Y. Liu, M.-K. Yang, W. Gao, Y.-Z. Zhang, L. Geng, D.-S. Zhang, S. Zhuang and X. Zhang, *Inorg. Chem. Commun.*, 2024, **170**, 113174.
185 L.-Z. Yang, W. Xie, L. Yan, Q. Fu, X. Yuan, Q. Zheng and X. Zhao, *Sep. Purif. Technol.*, 2024, **346**, 127513.
186 G.-R. Si, X.-J. Kong, T. He, Z. Zhang and J.-R. Li, *Nat. Commun.*, 2024, **15**, 7220.
187 M. Thommes, K. Kaneko, A. V. Neimark, J. P. Olivier, F. Rodriguez-Reinoso, J. Rouquerol and K. S. W. Sing, *Pure Appl. Chem.*, 2015, **87**, 1051–1069.
188 R. Vaidhyanathan, S. S. Iremonger, K. W. Dawson and G. K. H. Shimizu, *Chem. Commun.*, 2009, 5230.
189 W. Liu, Y. Zhang, S. Wang, L. Bai, Y. Deng and J. Tao, *Molecules*, 2021, **26**, 5267.
190 J.-R. Li, R. J. Kuppler and H.-C. Zhou, *Chem. Soc. Rev.*, 2009, **38**, 1477.

191 F. Elwinger, P. Pourmand and I. Furó, *J. Phys. Chem. C*, 2017, **121**, 13757–13764.
192 J. Zhang, T. Xia, D. Zhao, Y. Cui, Y. Yang and G. Qian, *Sens. Actuators, B*, 2018, **260**, 63–69.
193 J. L. Obeso, E. Martínez-Ahumada, A. López-Olvera, J. Ortiz-Landeros, H. A. Lara-García, J. Balmaseda, S. López-Morales, E. Sánchez-González, D. Solis-Ibarra, C. Leyva and I. A. Ibarra, *ACS Appl. Energy Mater.*, 2023, **6**, 9084–9091.
194 J. L. Obeso, V. B. López-Cervantes, C. V. Flores, A. Martínez, Y. A. Amador-Sánchez, N. S. Portillo-Velez, H. A. Lara-García, C. Leyva, D. Solis-Ibarra and R. A. Peralta, *Dalton Trans.*, 2024, **53**, 4790–4796.
195 L. Wang and Y. Chen, *Chem. Commun.*, 2020, **56**, 6965–6968.
196 Y. Xie, H. Ma, F. L. He, J. Chen, Y. Ji, S. Han and D. Zhu, *Analyst*, 2020, **145**, 4772–4776.
197 E. Martínez-Ahumada, A. López-Olvera, P. Carmona-Monroy, H. Díaz-Salazar, M. H. Garduño-Castro, J. L. Obeso, C. Leyva, A. Martínez, M. Hernández-Rodríguez, D. Solis-Ibarra and I. A. Ibarra, *Dalton Trans.*, 2022, **51**, 18368–18372.
198 E. Martínez-Ahumada, D. W. Kim, M. Wahiduzzaman, P. Carmona-Monroy, A. López-Olvera, D. R. Williams, V. Martis, H. A. Lara-García, S. López-Morales, D. Solis-Ibarra, G. Maurin, I. A. Ibarra and C. S. Hong, *J. Mater. Chem. A*, 2022, **10**, 18636–18643.
199 V. B. López-Cervantes, D. W. Kim, J. L. Obeso, E. Martínez-Ahumada, Y. A. Amador-Sánchez, E. Sánchez-González, C. Leyva, C. S. Hong, I. A. Ibarra and D. Solis-Ibarra, *Nanoscale*, 2023, **15**, 12471–12475.
200 V. B. López-Cervantes, D. Bara, A. Yañez-Aulestia, E. Martínez-Ahumada, A. López-Olvera, Y. A. Amador-Sánchez, D. Solis-Ibarra, E. Sánchez-González, I. A. Ibarra and R. S. Forgan, *Chem. Commun.*, 2023, **59**, 8115–8118.
201 V. B. López-Cervantes, A. López-Olvera, J. L. Obeso, I. K. Torres, E. Martínez-Ahumada, P. Carmona-Monroy, E. Sánchez-González, D. Solís-Ibarra, E. Lima, E. Jangodaz, R. Babarao, I. A. Ibarra and S. G. Telfer, *Chem. Mater.*, 2024, **36**, 2735–2742.
202 M. Wang, L. Guo and D. Cao, *Anal. Chem.*, 2018, **90**, 3608–3614.
203 V. B. López-Cervantes, M. L. Martínez, J. L. Obeso, C. García-Carvajal, N. S. Portillo-Vélez, A. Guzmán-Vargas, R. A. Peralta, E. González-Zamora, I. A. Ibarra, D. Solis-Ibarra, J. L. Woodliffe and Y. A. Amador-Sánchez, *Dalton Trans.*, 2025, **54**, 1646–1654.
204 N. Ingle, S. Mane, P. Sayyad, G. Bodkhe, T. AL-Gahouari, M. Mahadik, S. Shirsat and M. D. Shirsat, *Front. Mater.*, 2020, **7**, 93.
205 Q. Li, J. Wu, L. Huang, J. Gao, H. Zhou, Y. Shi, Q. Pan, G. Zhang, Y. Du and W. Liang, *J. Mater. Chem. A*, 2018, **6**, 12115–12124.
206 N. Ingle, P. Sayyad, M. Deshmukh, G. Bodkhe, M. Mahadik, T. Al-Gahouari, S. Shirsat and M. D. Shirsat, *Appl. Phys. A: Mater. Sci. Process.*, 2021, **127**, 157.
207 X. Zhang, Z. Zhai, J. Wang, X. Hao, Y. Sun, S. Yu, X. Lin, Y. Qin and C. Li, *ChemNanoMat*, 2021, **7**, 1117–1124.
208 Z. Zhai, X. Zhang, J. Wang, H. Li, Y. Sun, X. Hao, Y. Qin, B. Niu and C. Li, *Chem. Eng. J.*, 2022, **428**, 131720.
209 Z. Zhai, J. Wang, Y. Sun, X. Hao, B. Niu, H. Xie and C. Li, *Appl. Surf. Sci.*, 2023, **613**, 155772.
210 N. Huo, D. Li, S. Zheng and W. Deng, *Chem. Eng. J.*, 2022, **432**, 134317.
211 M. E. DMello, N. G. Sundaram, A. Singh, A. K. Singh and S. B. Kalidindi, *Chem. Commun.*, 2019, **55**, 349–352.
212 V. Chernikova, O. Yassine, O. Shekhah, M. Eddaoudi and K. N. Salama, *J. Mater. Chem. A*, 2018, **6**, 5550–5554.
213 C. H. Pham and F. Paesani, *Inorg. Chem.*, 2018, **57**, 9839–9843.
214 M. R. Tchalala, P. M. Bhatt, K. N. Chappanda, S. R. Tavares, K. Adil, Y. Belmabkhout, A. Shkurenko, A. Cadiau, N. Heymans, G. De Weireld, G. Maurin, K. N. Salama and M. Eddaoudi, *Nat. Commun.*, 2019, **10**, 1328.
215 M. Pamei and A. Puzari, *Nano-Struct. Nano-Objects*, 2019, **19**, 100364.
216 Z. Liao, T. Xia, E. Yu and Y. Cui, *Crystals*, 2018, **8**, 338.
217 M. Runowski, D. Marcinkowski, K. Soler-Carracedo, A. Gorczyński, E. Ewert, P. Woźny and I. R. Martín, *ACS Appl. Mater. Interfaces*, 2023, **15**, 3244–3252.
218 W. P. Lustig, S. Mukherjee, N. D. Rudd, A. V. Desai, J. Li and S. K. Ghosh, *Chem. Soc. Rev.*, 2017, **46**, 3242–3285.
219 Y. Liu, X.-Y. Xie, C. Cheng, Z.-S. Shao and H.-S. Wang, *J. Mater. Chem. C*, 2019, **7**, 10743–10763.
220 C. Yuan, S. Saito, C. Camacho, S. Irle, I. Hisaki and S. Yamaguchi, *J. Am. Chem. Soc.*, 2013, **135**, 8842–8845.
221 Y. Zheng, Y. Zhou, J. Yu, Y. Yu, H. Zhang and W. P. Gillin, *J. Phys. D: Appl. Phys.*, 2004, **37**, 531–534.
222 D. E. Williams and N. B. Shustova, *Chem. – Eur. J.*, 2015, **21**, 15474–15479.
223 S. Xing and C. Janiak, *Chem. Commun.*, 2020, **56**, 12290–12306.
224 M. Zeng, A. Ren, W. Wu, Y. Zhao, C. Zhan and J. Yao, *Chem. Sci.*, 2020, **11**, 9154–9161.
225 L. Chen, Y. Song, W. Liu, H. Dong, D. Wang, J. Liu, Q. Liu and X. Chen, *J. Alloys Compd.*, 2022, **893**, 162322.
226 L. Yu, H. Wang, W. Liu, S. J. Teat and J. Li, *Cryst. Growth Des.*, 2019, **19**, 6850–6854.
227 J. L. Mancuso, A. M. Mroz, K. N. Le and C. H. Hendon, *Chem. Rev.*, 2020, **120**, 8641–8715.
228 M. Ji, X. Lan, Z. Han, C. Hao and J. Qiu, *Inorg. Chem.*, 2012, **51**, 12389–12394.
229 M. Shen, Y. Zhang, H. Xu and H. Ma, *iScience*, 2021, **24**, 103069.
230 F. Ahmadijokani, H. Molavi, S. Tajahmadi, M. Rezakazemi, M. Amini, M. Kamkar, O. J. Rojas and M. Arjmand, *Coord. Chem. Rev.*, 2022, **464**, 214562.
231 J. Perego, I. Villa, A. Pedrini, E. C. Padovani, R. Crapanzano, A. Vedda, C. Dujardin, C. X. Bezuidenhout, S. Bracco, P. E. Sozzani, A. Comotti, L. Gironi, M. Beretta, M. Salomoni,

N. Kratochwil, S. Gundacker, E. Auffray, F. Meinardi and A. Monguzzi, *Nat. Photonics*, 2021, **15**, 393–400.
232 M. A. Chowdhury, *ChemBioEng Rev.*, 2017, **4**, 225–239.
233 J.-X. Wang, J. Yin, O. Shekhah, O. M. Bakr, M. Eddaoudi and O. F. Mohammed, *ACS Appl. Mater. Interfaces*, 2022, **14**, 9970–9986.
234 L. E. Kreno, K. Leong, O. K. Farha, M. Allendorf, R. P. Van Duyne and J. T. Hupp, *Chem. Rev.*, 2012, **112**, 1105–1125.
235 A. Mallick, A. M. El-Zohry, O. Shekhah, J. Yin, J. Jia, H. Aggarwal, A.-H. Emwas, O. F. Mohammed and M. Eddaoudi, *J. Am. Chem. Soc.*, 2019, **141**, 7245–7249.
236 K. Miyata, T. Nakagawa, R. Kawakami, Y. Kita, K. Sugimoto, T. Nakashima, T. Harada, T. Kawai and Y. Hasegawa, *Chem. – Eur. J.*, 2011, **17**, 521–528.
237 Y. Ming, N. Kumar and D. J. Siegel, *ACS Omega*, 2017, **2**, 4921–4928.
238 I.-D. Kim, A. Rothschild and H. L. Tuller, *Acta Mater.*, 2013, **61**, 974–1000.
239 M. G. Campbell, D. Sheberla, S. F. Liu, T. M. Swager and M. Dincă, *Angew. Chem., Int. Ed.*, 2015, **54**, 4349–4352.
240 V. Schroeder, S. Savagatrup, M. He, S. Lin and T. M. Swager, *Chem. Rev.*, 2019, **119**, 599–663.
241 L. Torsi, M. Magliulo, K. Manoli and G. Palazzo, *Chem. Soc. Rev.*, 2013, **42**, 8612.
242 Z. Hu, J. Miu, X. Zhang, M. Jia and J. Yao, *J. Appl. Polym. Sci.*, 2022, **139**, e52810.
243 P. V. Shinde and C. S. Rout, *Nanoscale Adv.*, 2021, **3**, 1551–1568.
244 A. Punnoose, K. M. Reddy, A. Thurber, J. Hays and M. H. Engelhard, *Nanotechnology*, 2007, **18**, 165502.
245 A. Punnoose, K. M. Reddy, J. Hays, A. Thurber and M. H. Engelhard, *Appl. Phys. Lett.*, 2006, **89**, 112509.
246 A. A. Bagade, V. V. Ganbavle, S. V. Mohite, T. D. Dongale, B. B. Sinha and K. Y. Rajpure, *J. Colloid Interface Sci.*, 2017, **497**, 181–192.
247 H. Goesmann and C. Feldmann, *Angew. Chem., Int. Ed.*, 2010, **49**, 1362–1395.
248 O. Kahn and C. J. Martinez, *Science*, 1998, **279**, 44–48.
249 C. Bartual-Murgui, A. Akou, C. Thibault, G. Molnár, C. Vieu, L. Salmon and A. Bousseksou, *J. Mater. Chem. C*, 2015, **3**, 1277–1285.
250 L. Wang, Z. Wang, Q. Xiang, Y. Chen, Z. Duan and J. Xu, *Sens. Actuators, B*, 2017, **248**, 820–828.
251 R. Paolesse, C. Di Natale, A. Macagnano, F. Davide, T. Boschi and A. D'Amico, *Sens. Actuators, B*, 1998, **47**, 70–76.
252 L. Zhang, Q. Yang and Z. Zhu, *Foods*, 2024, **13**, 1936.
253 X. Wang, J. Zhang, Z. Zhu and J. Zhu, *Appl. Surf. Sci.*, 2007, **253**, 3168–3173.
254 Y. Cui, Y. Yue, G. Qian and B. Chen, *Chem. Rev.*, 2012, **112**, 1126–1162.
255 C. Wu, H. Xu, Y. Li, R. Xie, P. Li, X. Pang, Z. Zhou, B. Gu, H. Li and Y. Zhang, *Talanta*, 2019, **200**, 78–83.
256 M.-S. Yao, W.-H. Li and G. Xu, *Coord. Chem. Rev.*, 2021, **426**, 213479.
257 R.-M. Neubieser, J.-L. Wree, J. Jagosz, M. Becher, A. Ostendorf, A. Devi, C. Bock, M. Michel and A. Grabmaier, *Micro Nano Eng.*, 2022, **15**, 100126.
258 M. Gupta, H. Hawari, P. Kumar and Z. Burhanudin, *Crystals*, 2022, **12**, 264.
259 H. S. Magar, R. Y. A. Hassan and A. Mulchandani, *Sensors*, 2021, **21**, 6578.
260 V. Balasubramani, S. Sureshkumar, T. S. Rao and T. M. Sridhar, *ACS Omega*, 2019, **4**, 9976–9982.
261 B. Zong, Q. Li, X. Chen, C. Liu, L. Li, J. Ruan and S. Mao, *ACS Appl. Mater. Interfaces*, 2020, **12**, 50610–50618.
262 A. Paghi, S. Mariani and G. Barillaro, *Small*, 2023, **19**, 2206100.
263 J. Park, H. Kim and Y. Jung, *J. Phys. Chem. Lett.*, 2013, **4**, 2530–2534.
264 M. Mukoyoshi, M. Maesato, S. Kawaguchi, Y. Kubota, K. Cho, Y. Kitagawa and H. Kitagawa, *Inorg. Chem.*, 2022, **61**, 7226–7230.
265 C. Zhai, Q. Zhao, K. Gu, D. Xing and M. Zhang, *J. Alloys Compd.*, 2019, **784**, 660–667.
266 H. Yuan, J. Tao, N. Li, A. Karmakar, C. Tang, H. Cai, S. J. Pennycook, N. Singh and D. Zhao, *Angew. Chem., Int. Ed.*, 2019, **58**, 14089–14094.